# Phosphoproteomics reveals rewiring of the insulin signaling network and multi-nodal defects in insulin resistance

Daniel J. Fazakerley[1,2]#*, Julian van Gerwen[1]#, Kristen C. Cooke[1], Xiaowen Duan[1], Elise J. Needham[1], Søren Madsen[1], Dougall M. Norris[2], Amber S. Shun-Shion[2], James R. Krycer[1,5,6], James G. Burchfield[1], Pengyi Yang[3,4], Mark R. Wade[7], Joseph T. Brozinick[7], David E. James[1,8]*, Sean J. Humphrey[1, 9]*

1. Charles Perkins Centre, School of Life and Environmental Sciences, University of Sydney, 2006, Australia
2. Metabolic Research Laboratories, Wellcome-Medical Research Council Institute of Metabolic Science, University of Cambridge, Cambridge, CB2 0QQ, UK
3. Charles Perkins Centre, School of Mathematics and Statistics, University of Sydney, NSW, 2006, Australia
4. Computational Systems Biology Group, Children's Medical Research Institute, Faculty of Medicine and Health, University of Sydney, Westmead, NSW, 2145, Australia
5. QIMR Berghofer Medical Research Institute, Brisbane, Queensland, Australia
6. Faculty of Health, School of Biomedical Sciences, Queensland University of Technology, Australia
7. Lilly Research Laboratories, Division of Eli Lilly and Company, Indianapolis, IN, USA.
8. Sydney Medical School, University of Sydney, Sydney, 2006, Australia
# These authors contributed equally.
* Correspondence: sean.humphrey@sydney.edu.au, david.james@sydney.edu.au, djf72@medschl.cam.ac.uk

## Abstract

The failure of metabolic tissues to appropriately respond to insulin ("insulin resistance") is an early marker in the pathogenesis of type 2 diabetes. Protein phosphorylation is central to the adipocyte insulin response, but how adipocyte signaling networks are dysregulated upon insulin resistance is unknown. Here we employed phosphoproteomics to delineate insulin signal transduction in adipocyte cells and adipose tissue. Across a range of insults triggering insulin resistance, we observed marked rewiring of the insulin signaling network. This included both attenuated insulin-responsive phosphorylation, and the emergence of phosphorylation uniquely insulin-regulated in insulin resistance. Identifying signaling changes common to multiple insults revealed subnetworks likely containing causal drivers of insulin resistance. Focusing on defective GSK3 signaling initially observed in a relatively small subset of well-characterized substrates, we employed a pipeline for identifying context-specific kinase substrates. This facilitated robust identification of widespread dysregulated GSK3 signaling. Pharmacological inhibition of GSK3 partially reversed insulin resistance in cells and tissue explants. These data highlight that insulin resistance is a multi-nodal signaling defect that encompasses dysregulated GSK3 activity.

## Main

Insulin resistance is a key defect preceding type 2 diabetes, cardiovascular disease, and other metabolic diseases[1]. Impaired insulin-stimulated translocation of the glucose transporter GLUT4 to the cell surface is one of the primary defects resulting from insulin resistance in muscle and adipose tissue, leading to decreased insulin-stimulated glucose uptake[1]. Adipose tissue insulin resistance precedes muscle insulin resistance during high-fat feeding[2,3], and adipose-specific abrogation of insulin action leads to systemic insulin resistance[4,5]. Hence, there is considerable interest in studying adipose insulin action to understand how this tissue contributes to whole-body insulin resistance. Reversible protein phosphorylation is an essential post-translational modification mediating insulin action, making signal transduction a focal point for mechanistic understanding of this metabolic process[6].

Adipose insulin resistance has been linked to external stressors including chronic inflammation[7], hyperinsulinemia[8], glucocorticoids[9], and lipotoxicity[10,11], as well as associated internal stressors such as mitochondrial dysfunction[12], oxidative stress[13], and endoplasmic reticulum stress[14]. These stressors have been suggested to impair early steps in the insulin signaling cascade, thereby attenuating insulin-stimulated GLUT4 translocation. Indeed, several protein kinases activated by these insults, including mTORC1, S6K, Jnk and PKC, have been reported to phosphorylate and inhibit the insulin receptor or its scaffold protein IRS (reviewed in[15]). However, this hypothesis has recently been called into question[1,16], and the causal relationship between changes in early insulin signaling and the downstream actions of insulin remains unclear, especially in the context of insulin resistance. There is therefore an urgent need for global unbiased analyses of signaling in insulin resistant cells to pinpoint potential alterations contributing to insulin resistance.

Mass spectrometry (MS)-based phosphoproteomics now makes it possible to study insulin signaling on a global scale[17–19]. Here, we employed recent advances in the throughput and sensitivity of these technologies[20,21] to analyze acute signaling responses to insulin in the

context of adipose insulin resistance. We initially focused on the highly insulin-responsive 3T3-L1 adipocyte cell line allowing us to study signaling defects in isolation from the complex milieu of whole organisms, and subsequently validated key findings in mouse adipose tissue. In particular we exposed cells to five insults spanning a broad range of factors known to contribute to adipocyte insulin resistance, reasoning that signaling changes induced by multiple insults would be more likely to contribute to the etiology of insulin resistance.

Our global phosphoproteomic analyses reveal that insulin resistance is accompanied by extensive rewiring of the insulin signaling network. A diverse subnetwork of kinases, proteins, and pathways were dysregulated across the models, while canonically studied insulin signaling nodes remained largely intact. Using a small molecule inhibitor together with phosphoproteomics and motif analysis we generated a resource of adipocyte-specific substrates for the kinase GSK3. This approach facilitated the identification of defective GSK3 signalling across all cell models, and in insulin resistant adipose tissue. Studies in cells and tissues using GSK3 inhibitors established that acute GSK3 inhibition partially restored insulin sensitivity, supporting these findings. Thus, our data provide a quantitative atlas delineating the signaling dysregulation in adipocytes during insulin resistance and can be navigated at www.adipocyteatlas.org.

## Results

### *Establishing proteomic and phosphoproteomic models of adipocyte insulin resistance*

We selected five distinct models of insulin resistance in 3T3-L1 adipocytes, enabling us to pinpoint molecular rearrangements specific to insulin resistance rather than side-effects of the insults that cause it. These included three well-characterized models mimicking systemic insults reported to induce insulin resistance in humans and animals: hyperinsulinemia (chronic insulin treatment, **CI**), glucocorticoids (dexamethasone treatment, **DEX**) and inflammation (TNFα treatment, **TNF**) (**Fig. 1A**)[3]. Mitochondrial oxidants have recently been implicated in

insulin resistance[3,22,23], and we therefore included two models comprising the acute (2h) production of mitochondrial oxidants from different sources (mitochondria-targeted paraquat, **MPQ**, antimycin A, **AA**) (**Fig. 1A**)[22,23]. All five models conferred impaired uptake of radiolabeled 2-deoxyglucose (2DG) into adipocyte cells following an acute (10 min) insulin treatment, confirming that cells were insulin resistant (**Fig. 1B**).

We assessed changes in protein expression and insulin signaling responses in control and insulin resistant adipocytes by mass spectrometry-based proteomic and phosphoproteomic analyses (**Fig. 1C**). Together we quantified 7,564 proteins across all models (**Fig. 1D**), as well as 39,846 phosphopeptides corresponding to 29,311 phosphorylation sites on 3,791 proteins (**Fig. 1E**). Our proteomic and phosphoproteomic data were very high quality, revealed by Pearson's correlation, principal component analysis, and hierarchical clustering, with samples from the same model and insulin-stimulation status highly correlated (average Pearson's correlation; proteome r = 0.96, phosphoproteome r = 0.89), and clustered together (**Fig. S1A-F**). We also observed no major differences in the number of quantified phosphopeptides between conditions (**Fig. S1G-H**). Together, this demonstrates that our MS data are both accurate and reproducible. While unstimulated and insulin-stimulated samples from the same model clustered distinctly when considering the phosphoproteome data (**Fig. S1A, E**), they clustered together in the proteome data (**Fig. S1B, F**), indicating that the proteome was unchanged in the short 10 min insulin treatment, as expected. Accordingly, we detected no statistically significant changes to the proteome upon the short insulin treatment across all models (**Data S1**).

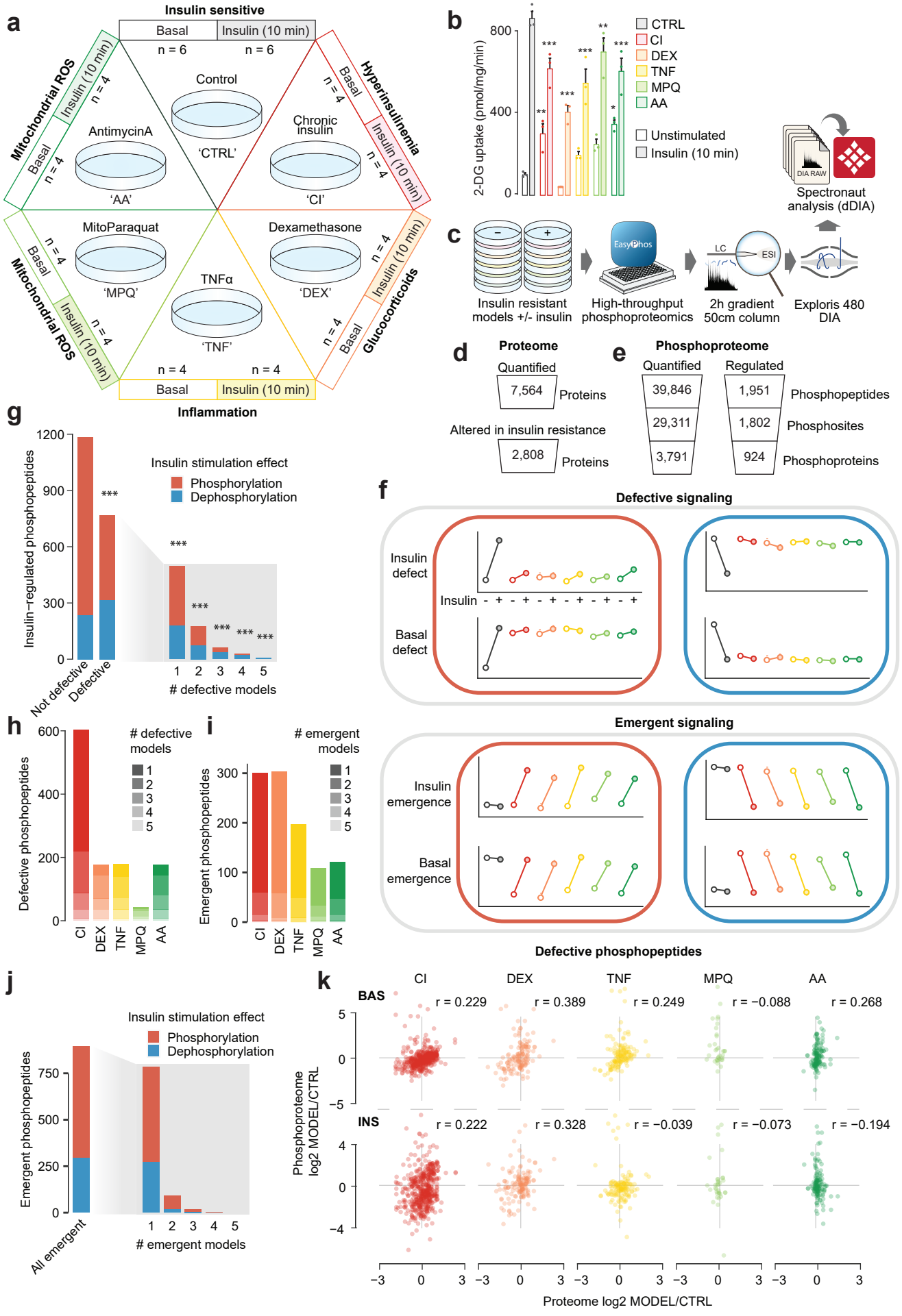
a
Insulin sensitive
Basal
Insulin (10 min)
n = 6
n = 6
Control
'CTRL'
Mitochondrial ROS
Insulin (10 min)
n = 4
Basal
n = 4
AntimycinA
'AA'
Hyperinsulinemia
Basal
n = 4
Insulin (10 min)
n = 4
Chronic insulin
'CI'
Mitochondrial ROS
n = 4
Basal
n = 4
Insulin (10 min)
MitoParaquat
'MPQ'
TNFα
'TNF'
Glucocorticoids
n = 4
Insulin (10 min)
n = 4
Basal
Dexamethasone
'DEX'
n = 4
Basal
n = 4
Insulin (10 min)
n = 4
n = 4
Basal
Insulin (10 min)
Inflammation
b
2-DG uptake (pmol/mg/min)
800
400
0
CTRL
CI
DEX
TNF
MPQ
AA
Unstimulated
Insulin (10 min)
DIA RAW
Spectronaut analysis (dDIA)
c
Insulin resistant models +/- insulin
EasyPhos
High-throughput phosphoproteomics
LC
ESI
2h gradient 50cm column
Exploris 480 DIA
d
Proteome
Quantified
7,564
Proteins
Altered in insulin resistance
2,808
Proteins
e
Phosphoproteome
Quantified
39,846
29,311
3,791
Regulated
1,951
1,802
924
Phosphopeptides
Phosphosites
Phosphoproteins
f
Defective signaling
Insulin defect
Insulin - + - + - + - + - + - +
Basal defect
Emergent signaling
Insulin emergence
Basal emergence
g
Insulin−regulated phosphopeptides
1200
900
600
300
0
Insulin stimulation effect
Phosphorylation
Dephosphorylation
***
***
***
***
***
***
1 2 3 4 5
# defective models
Not defective
Defective
h
Defective phosphopeptides
600
400
200
0
# defective models
1
2
3
4
5
CI
DEX
TNF
MPQ
AA
i
Emergent phosphopeptides
300
200
100
0
# emergent models
1
2
3
4
5
CI
DEX
TNF
MPQ
AA
Defective phosphopeptides
j
Emergent phosphopeptides
750
500
250
0
Insulin stimulation effect
Phosphorylation
Dephosphorylation
1 2 3 4 5
# emergent models
All emergent
k
CI
DEX
TNF
MPQ
AA
BAS
r = 0.229
r = 0.389
r = 0.249
r = −0.088
r = 0.268
INS
r = 0.222
r = 0.328
r = −0.039
r = −0.073
r = −0.194
Phosphoproteome log2 MODEL/CTRL
5
0
−5
4
0
−4
−3
0
3
Proteome log2 MODEL/CTRL

***Fig 1: Analysis of the proteome and phosphoproteome of insulin resistant adipocytes***

(**A**) Adipocyte insulin resistance models and sample sizes. (**B**) $^{3}$H-2DG uptake into insulin resistant adipocytes at 37 °C or 4 °C after 10 min. Data analyzed by two-way ANOVA corrected for multiple comparisons (Dunnett's test), control vs insulin resistant models in unstimulated or stimulated cells (*). Error bars are S.E.M., n = 3. (**C**) Workflow for 3T3-L1 adipocyte insulin resistance phosphoproteomes. (**D-E**) Quantification from (**D**) proteomic and (**E**) phosphoproteomic analysis of insulin resistant adipocytes. "Altered in insulin resistance" refers to proteins changed in ≥ 1 models compared to control, and "Regulated" to phosphopeptides regulated by insulin in control cells. (**H**) Theoretical depiction of two ways in which insulin-stimulated protein phosphorylation can change in insulin resistance. (**G**) Distribution of insulin resistance defects among phosphopeptides regulated by insulin in control cells. Phosphopeptides separated by whether or not they are defective in at least one insulin resistance model (Defective). The maximum number of models in which each phosphopeptide is defective is shown. One-sided Fisher's exact tests were performed to assess whether phosphopeptides defective in at least 1, 2, 3, 4, or 5 models were more likely to be dephosphorylated in control cells (p-values corrected by Benjamini-Hochberg (*'s)). (**H**) Number of insulin-regulated phosphopeptides defective in each model. (**I-J**) The distribution of emergent phosphopeptides. (**K**) Correlation of proteome and unstimulated (BAS) or insulin-stimulated (INS) phosphoproteome changes in phosphopeptides with defective phosphorylation in the indicated models. r = pearson's correlation coefficient. *: $0.01 < p < 0.05$, **: $0.001 < p < 0.01$, ***: $p < 0.001$.

### *Characterization of the insulin-resistant proteome*

Analysis of the proteome revealed that 37% of proteins were significantly changed in at least one model of insulin resistance (Dunnett's post-hoc adj. $p < 0.05$, Model/CTRL > 1.5, 1,398 up-regulated and 1,410 down-regulated proteins, **Fig. S1I, Data S1**). This included 1,693 differentially expressed proteins in CI, 1,621 in DEX and 1,019 in TNF **(Fig. S1J, K, Data S1)**. In contrast, only 12 proteins were differentially regulated in response to MPQ or AA (nine in MPQ, nine in AA, and six in both). Proteomic changes in CI, DEX and TNF were consistent with those previously reported[3]. For example, GLUT4 (SLC2A4) and AKT2 were down-regulated (**Fig. S1K, Data S1**), and proteins in pathways such as peroxisome proliferator-activated receptor signaling, insulin signaling, lipid metabolism (fatty acid metabolism, biosynthesis of unsaturated fatty acids, the mevalonate/terpenoid backbone biosynthesis pathway, cholesterol biosynthesis), branched chain amino acid metabolism (valine, leucine, and isoleucine degradation) and oxidative phosphorylation were altered (**Fig. S2A, B**). In general, these pathways also behave similarly in the transcriptome of related models[24]. To identify functionally associated proteins with altered expression in insulin resistance, we extracted protein-protein interaction (PPI) data from STRING[25] for networks comprising proteins up- or down-regulated in two or more models (388 up-regulated, 621 down-regulated). This revealed PPI clusters enriched in spliceosomal- (up-regulated), endocytic- (up-regulated) and ribosomal- (up- and down-regulated) proteins, suggesting that these protein networks are sensitive to multiple perturbations that elicit insulin resistance (**Fig. S2C, D**, **Data S2**). Thus, our deep proteome analysis confirms previous reports of extensive changes in protein expression across multiple models of insulin resistance and provides a quantitative atlas for studies into underlying causes of insulin resistance.

### *Insulin resistance rewires the insulin signaling network*

The absence of widespread changes to the proteome in our acute models (MPQ, AA; 2h) emphasizes that insulin resistance in these models is unlikely to be driven at the level of protein

expression. This further prompted us to consider changes to global protein phosphorylation networks, which have been shown to operate on much faster timescales than both transcriptional and translational machinery[26]. In our phosphoproteomics data we detected 1,951 insulin-regulated phosphopeptides in control cells that had altered abundance following insulin treatment (log2 fold-change > 0.58 or < -0.58, adj. $p$ < 0.05) (**Data S3**). Among these phosphopeptides were numerous known insulin-responsive phosphorylation sites serving as positive controls. These included AKT1S1 T247, RPS6 S235/236, MTOR S2481, MAPK1 Y185, MAPK3 T203/Y205, GYS1 S641 and TBC1D4 S595 (**Fig. S3A, Data S3**).

We next considered how changes in protein phosphorylation could contribute to insulin resistance (**Fig. 1F**). One mode is 'defective phosphorylation', whereby insulin increases or decreases the abundance of a phosphosite in control cells but fails to do so in insulin resistance. As insulin modulates protein phosphorylation to enact its functional outcomes such as GLUT4 translocation, defects in insulin-regulated phosphorylation could lead to insulin resistance. In the case of a phosphosite normally increased by insulin, a defect could be due to the failure of insulin to increase the phosphosite to appropriate levels (insulin defect), or because the phosphosite is already elevated prior to the addition of insulin (basal defect) (**Fig. 1F**). Another mode of dysregulation we considered is 'emergent phosphorylation', whereby a phosphosite is not altered by insulin in control conditions but becomes regulated by insulin only in insulin resistance (**Fig. 1F**). Emergent signaling events that counteract the canonical functions of insulin could contribute to the etiology of insulin resistance.

We first examined defective phosphorylation. Remarkably, 767 of the 1,951 insulin-responsive phosphopeptides detected in control cells were not regulated by insulin in one or more insulin resistant models (**Fig. 1G**). The extent of these defects varied substantially between models, from 604 phosphopeptides dysregulated in CI, to only 43 in MPQ (**Fig. 1H**). Only 128 of these 1,951 phosphopeptides were defective in three or more models, and just seven were defective in all models (**Data S3**, **Fig. 1G**). This supports the view that a single insult may cause many

changes to signaling networks not specific to insulin resistance, highlighting the utility of studying multiple models. Although we observed widespread defects in insulin signaling, even more phosphopeptides displayed an emergent response to insulin in one or more models (896 phosphopeptides, **Fig. 1I, J**). This indicates that insults causing insulin resistance do not just attenuate insulin signaling, rather they rewire the insulin-responsive signaling network. Emergent signaling events were less well conserved between models compared to defective signaling, with only 19 sites emergent in three or more models (**Fig. 1I, J**).

Comparative analysis of our deep proteome and phosphoproteomes of each model provides the opportunity to explore whether altered signaling coincided with changes in protein abundance. To this end, we correlated phosphopeptide and protein abundance changes in each model compared to control cells for defective phosphopeptides (**Fig. 1K**) or emergent phosphopeptides (**Fig. S3B**). In all models, and regardless of insulin stimulation status, we observed poor correlation between changes in phosphopeptide and protein expression. This suggests that signaling changes were largely independent from changes in kinase-substrate kinetics driven by alterations in protein expression. Overall, our findings imply that insulin resistance substantially rewires the insulin signaling network, and this is generally not due to equivalent changes in protein levels.

***Profiling kinase regulation in insulin resistance***

Mechanistically, changes in signaling observed in insulin resistance could be caused by the dysregulation of one or more protein kinases. To identify potential kinases involved, we performed kinase substrate enrichment analysis (KSEA)[27], which assessed kinase activation profiles across the insulin resistance models using the insulin response of previously annotated kinase substrates (PhosphositePlus[28], **Fig. 2A**). KSEA recapitulated the known activation profiles of multiple kinases in insulin-responsive control cells, including AKT, mTOR, p70S6K, JNK, and ERK[29,30]. p70S6K is activated by mTOR in response to insulin, and the activation profiles of both kinases were highly correlated across models, indicating that our

analysis accurately captured kinase regulatory patterns. However, this approach is constrained to kinases with an abundance of high-quality, context-relevant substrate annotations. This is exemplified by the fact that GSK3 was erroneously reported by KSEA to be activated by insulin in control cells, while it is known that insulin inhibits GSK3 through phosphorylation by AKT[31] at key sites. Indeed, phosphorylation of these canonical AKT inhibitory sites on GSK3α (S21) and GSK3β (S9) were robustly increased in response to insulin in control cells (**Fig. 2B**). As PhosphositePlus annotations are aggregated from different experimental designs (for example *in vitro* and *in vivo* assays) and from different systems (for example different cell lines and conditions), we surmised that a subset of the annotated GSK3 substrates were not regulated by GSK3 in our experimental system. This underscores the importance of mapping high-quality kinase substrates relevant to a particular biological context.

Two kinases displayed impaired insulin-activation in three or more insulin resistance models, ERK (CI, TNF, AA), and CDK5 (CI, TNF, MPQ, AA, **Fig. 2A**). Accordingly, insulin-stimulated phosphorylation of the MAPK3/ERK1 and MAPK1/ERK2 activation sites were significantly attenuated in CI, TNF, and AA compared to CTRL (**Fig. S3C**). These results support previous findings that ERK activation is either defective[32] or intact[33] in skeletal muscle insulin resistance, but do not support the common view that insulin resistance is mediated by ERK hyperactivity[34–37]. CDK5 activation has been implicated in insulin-stimulated glucose uptake[38], supporting a putative role for CDK5 dysregulation in insulin resistance. Collectively, this analysis suggests impaired insulin-activation of ERK and CDK5 may contribute to insulin resistance.

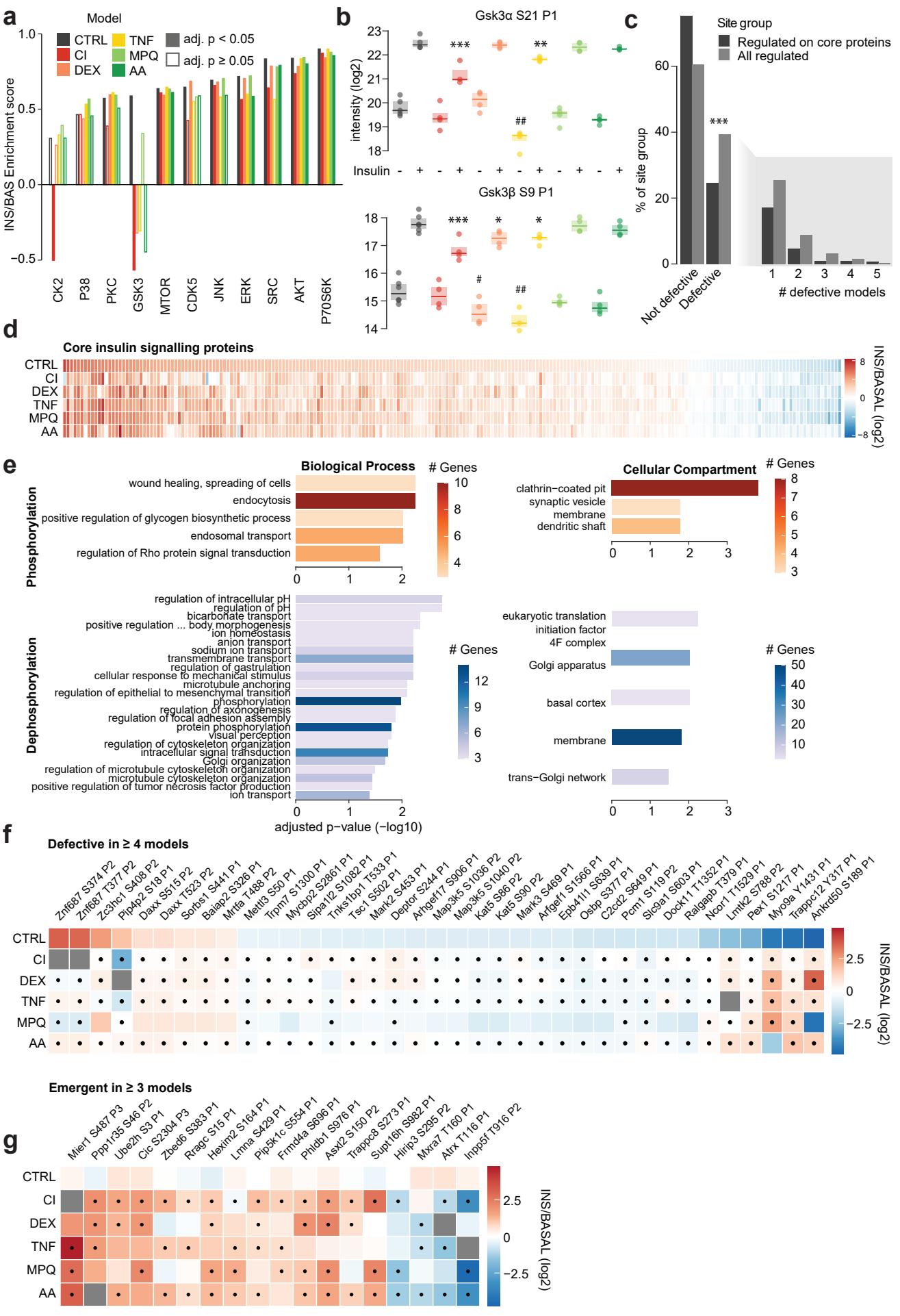
a
Model
CTRL
CI
DEX
TNF
MPQ
AA
adj. p < 0.05
adj. p ≥ 0.05
INS/BAS Enrichment score
CK2
P38
PKC
GSK3
MTOR
CDK5
JNK
ERK
SRC
AKT
P70S6K
b
Gsk3α S21 P1
intensity (log2)
Insulin
Gsk3β S9 P1
c
Site group
Regulated on core proteins
All regulated
% of site group
Not defective
Defective
# defective models
d
Core insulin signalling proteins
INS/BASAL (log2)
e
Biological Process
# Genes
wound healing, spreading of cells
endocytosis
positive regulation of glycogen biosynthetic process
endosomal transport
regulation of Rho protein signal transduction
Phosphorylation
Cellular Compartment
clathrin−coated pit
synaptic vesicle
membrane
dendritic shaft
regulation of intracellular pH
regulation of pH
bicarbonate transport
positive regulation ... body morphogenesis
ion homeostasis
anion transport
sodium ion transport
transmembrane transport
regulation of gastrulation
cellular response to mechanical stimulus
microtubule anchoring
regulation of epithelial to mesenchymal transition
phosphorylation
regulation of axonogenesis
regulation of focal adhesion assembly
protein phosphorylation
visual perception
regulation of cytoskeleton organization
intracellular signal transduction
Golgi organization
regulation of microtubule cytoskeleton organization
microtubule cytoskeleton organization
positive regulation of tumor necrosis factor production
ion transport
Dephosphorylation
adjusted p−value (−log10)
eukaryotic translation initiation factor 4F complex
Golgi apparatus
basal cortex
membrane
trans−Golgi network
f
Defective in ≥ 4 models
Znf687 S374 P2
Znf687 T377 P2
Zc3hc1 S408 P2
Pip4p2 S18 P1
Daxx S515 P2
Daxx T523 P2
Sorbs1 S441 P1
Baiap2 S326 P1
Mrtfa T488 P2
Mettl3 S50 P1
Trpm7 S1300 P1
Mycbp2 S2861 P1
Sipa1l2 S1082 P1
Tnks1bp1 T533 P1
Tsc1 S502 P1
Mark2 S453 P1
Deptor S244 P1
Arhgef17 S906 P1
Map3k5 S1036 P2
Map3k5 S1040 P2
Kat5 S86 P2
Kat5 S90 P2
Mark3 S469 P1
Arfgef1 S1566 P1
Epb41l1 S639 P1
Osbp S377 P1
C2cd2 S649 P1
Pcm1 S119 P2
Stc9a1 S603 P1
Dock11 T1352 P1
Ralgapb T379 P1
Ncor1 T1529 P1
Lmtk2 S788 P2
Pex1 S1217 P1
Myo9a Y1431 P1
Trappc12 Y317 P1
Ankrd50 S189 P1
Emergent in ≥ 3 models
Mier1 S487 P3
Ppp1r35 S46 P2
Ube2h S3 P1
Cic S2304 P3
Zbed6 S383 P1
Rragc S15 P1
Heximr2 S164 P1
Lmna S429 P1
Pip5k1c S554 P1
Frmd4a S696 P1
Phldb1 S976 P1
Asxl2 S150 P2
Trappc8 S273 P1
Supt16h S982 P1
Hirip3 S295 P2
Mxra7 T160 P1
Atrx T116 P1
Inpp5f T916 P2

***Fig 2: Impaired and emergent signaling in insulin resistance***

(**A**) Kinase substrate enrichment analysis (KSEA) was performed in each insulin resistance model to assess the regulation of kinases by insulin using log2 INS/BAS fold changes. Columns are filled in for significantly regulated kinases (Benjamini-Hochberg-adjusted $p < 0.05$). Only kinases significantly regulated in at least one model are displayed. (**B**) Intensity of GSK3α S21 and, GSK3β S9 phosphopeptides. "P1" indicates both phosphopeptides contained only one phosphosite. ANOVAs and Dunnett's post hoc tests performed unstimulated (#) or insulin-stimulated (*) phosphoproteome data, insulin resistant models vs control cells. *: $0.01 < p < 0.05$, **: $0.001 < p < 0.01$, ***: $p < 0.001$. (**C**) The distribution of phosphorylation defects among regulated phosphopeptides on all proteins or on proteins considered part of the core insulin signaling pathway. One-sided Fisher's exact test was performed to assess whether regulated phosphopeptides on core insulin signaling protein were less likely to be defective than expected by chance (*). (**D**) Phosphopeptides on core insulin signaling pathway proteins that were quantified in every condition. (**E**) Significantly enriched pathways from GO enrichment on genes contain insulin up-regulated (red) or down-regulated (blue) phosphopeptides. Colour indicates the number of phospho-dysregulated genes in each pathway. Abbreviated pathway is "positive regulation of basement membrane assembly involved in embryonic body morphogenesis". (**F-G**) Phosphopeptides that were (**F**) defective in four or more insulin resistance models or (**G**) emergent in three or more models. Dots indicate that model insulin responses were significantly different to control insulin responses. Ppp2r5b S13 was excluded from (**G**) to optimize the heatmap scale and is shown in Fig. S3F. *: $0.01 < p < 0.05$, **: $0.001 < p < 0.01$, ***: $p < 0.001$.

### *Characterizing defective and emergent insulin signaling*

Most studies reporting altered insulin signaling during insulin resistance have focused on canonical insulin signaling intermediates such as AKT[1,16]. Our global analysis did reveal that several phosphopeptides from proteins considered part of the canonical 'insulin signaling pathway' (defined in **Data S4**) were defective across multiple models of insulin resistance, including S502 on TSC1 and S244 on DEPTOR (**Fig. S3D**). However, KSEA revealed that AKT, the key regulator of insulin-stimulated GLUT4 translocation and glucose transport[29], and downstream kinases mTOR and p70S6K, were activated to a similar degree in control and insulin resistant cells (**Fig. 2A**). Moreover, insulin signaling to proteins comprising the canonical insulin signaling pathway remained intact in insulin resistant cells, as insulin-regulated phosphopeptides from these proteins were 1.7 times less likely to be defective than those on proteins outside of this pathway (**Fig. 2C, D**, one-sided Fisher's exact test: p = 6.736e-09). Overall, dysregulation within the core insulin signaling pathway was limited.

We next considered broader characteristics of the insulin resistance signaling network. Phosphopeptides defective in two or more models (271 phosphopeptides; 211 proteins) were enriched for proteins in processes such as "endocytosis", "focal adhesion assembly", and "transmembrane transport", and in cellular compartments such as the "golgi apparatus" and "membranes", highlighting these as potential sites of insulin resistance (**Fig. 2E**). While control cells exhibited a greater proportion of increased protein phosphorylation than decreased phosphorylation (1,402 increased phosphopeptides, 459 decreased phosphopeptides), insulin-regulated dephosphorylation was preferentially impaired in insulin resistance (**Fig. 1G**). Specifically, protein dephosphorylation was 1.8 times more likely to be defective in one or more models compared to phosphorylation (one-sided Fisher's exact test: adj. p = 1.411703e-23), and 4.6 times more likely to be defective in three or more models (p = 3.503999e-14, **Fig. 1G**). These instances of defective dephosphorylation were generally caused by changes in the insulin-stimulated phosphoproteome (insulin defect) rather than the unstimulated

phosphoproteome (basal defect) (**Fig. 1F, S3E**). This was also observed for defective phosphorylation (**Fig. 1F, S3E**). Together, these data suggest that impaired decreases in phosphorylation is a defining feature of insulin resistance.

Finally, we attempted to pinpoint individual phosphosites likely to contribute to insulin resistance. Among the 37 phosphopeptides defective in four or more models, several had regulatory roles such as S86 on Kat5, which promotes autophagy[39] and apoptosis[40], and S1040 on the stress and reactive oxygen species-sensitive kinase Map3k5/Ask1, which inhibits Ask1 activity and apoptosis[41] (**Fig. 2F**). Both were down-regulated by insulin in control cells. Genetic variants in Ask1 are associated with insulin resistance and type 2 diabetes in Pima Indians[42], further supporting a role for Ask1 in insulin resistance. We also observed sites of unknown function on proteins potentially involved in GLUT4 trafficking, including S411 on Sorbs1, a signaling adaptor that links the activated insulin receptor to lipid rafts and promotes GLUT4 translocation[43]; S603 on Slc9a1, a Na H+ exchanger that promotes actin rearrangement following activation by insulin[44]; T533 on Tnks1bp1 which is an interactor of Tankyrase, an insulin-activated GLUT4 vesicle-interactor required for GLUT4 translocation[45,46]; and Y317 on Trappc12 which is part of TRAPP, a complex involved in ER to Golgi trafficking[47]. There were 19 emergent sites in three or more models, including an uncharacterised site on pleckstrin homology-like domain family B member 1 (PHLDB1), a regulator of insulin-stimulated GLUT4 translocation[48] (**Fig. 2G, S3F**). Proteins possessing sites with emergent phosphorylation in three or more models were enriched in the GO terms “negative regulation of transcription and RNA polymerase II”; and “negative regulation of transcription, DNA-templated”, suggesting altered transcriptional regulation is a key target of signaling changes in insulin-resistant cells (**Fig. S3G**).

In all, rewiring of the insulin signaling network was largely exclusive of well-studied insulin signaling proteins. Instead, changes observed comprised a set of kinases, proteins, and pathways without known links with insulin at present. This suggests our knowledge of the

extent of mechanistic insulin signaling remains far from complete. Our data also imply that multiple parallel signaling alterations may cumulatively contribute to insulin resistance. If this is the case, targeting a single kinase or pathway may only confer a partial benefit to insulin sensitivity.

***Targeted analysis of the de-phosphorylation defect in adipocytes***

We observed that insulin-regulated dephosphorylation was widely dysregulated in all 3T3-L1 insulin resistance models (**Fig. 1G**). Acute phosphatase inhibition impaired insulin-stimulated 2DG uptake in 3T3-L1 adipocytes and adipose explants, and HA-GLUT4 translocation in 3T3-L1 adipocytes (**Fig. S4A-C**) as previously reported[49], supporting the notion that protein dephosphorylation is important to insulin action. However, we detected no change in global phosphatase activity in the CI, DEX or TNF models (**Fig. S4D**), and changes in the expression of specific phosphatases were limited to chronic models of insulin resistance (CI, DEX, TNF) and not acute models (AA, MPQ) (**Fig. S4E**). Therefore, we hypothesized that the defective insulin-stimulated protein dephosphorylation observed in multiple models of insulin resistance may be driven by aberrant kinase deactivation by insulin.

One of the best-known kinases inactivated by insulin is glycogen synthase kinase 3 (GSK3). Under normal conditions GSK3 is constitutively active, and its phosphorylation by AKT at Ser9/21 inactivates the kinase[31]. Several bona fide GSK3 substrates displayed impaired dephosphorylation across insulin resistance models, such as S641 on glycogen synthase (CI and AA), and S86 and S90 on the histone acetyltransferase Kat5 (CI, DEX, TNF, and AA) (**Fig. S4F**). In contrast, while PKA is also inactivated by insulin, we only found one annotated PKA substrate with defective dephosphorylation (Sik3 S493), which was only defective in a single model (DEX, **Fig. S4G**). These observations suggested that dysregulation of GSK3 activity may contribute to impaired dephosphorylation in insulin resistance.

As noted, our earlier KSEA using existing database annotations failed to accurately assess GSK3 activity (**Fig. 2A**). We therefore took this opportunity to establish a pipeline to identify a high-quality list of putative GSK3 substrates in adipocytes (**Fig. 3A**), reasoning that this knowledge would facilitate a more accurate evaluation of GSK3 activity in insulin resistance. To this end, we generated a phosphoproteome in 3T3-L1 adipocytes comprising 14,778 phosphopeptides. Of these, 849 (on 395 proteins) were responsive to acute treatment with the highly selective GSK3 inhibitor LY2090314 (hereafter referred to as "GSK3i")[50], with 309 phosphopeptides increasing and 381 decreasing (adj. $p < 0.05$, log2 fold-change > 0.58 or < -0.58 respectively) (**Fig. 3B, C**). To enrich these data for sites more likely to be direct substrates of GSK3 in adipocytes (as opposed to downstream of GSK3), we selected only those that were down-regulated in response to GSK3i and also contained the motif of a GSK3 substrate (pS/TXXXpS/T). The resulting 290 phosphopeptides corresponded to 274 phosphosites on 184 proteins (**Fig. 3B, C, Data S5**), and contained previously identified GSK3 targets such as S641, S645 and S649 on glycogen synthase[51], and S514 and S518 on DPYSL2[52,53], confirming the validity of our approach.

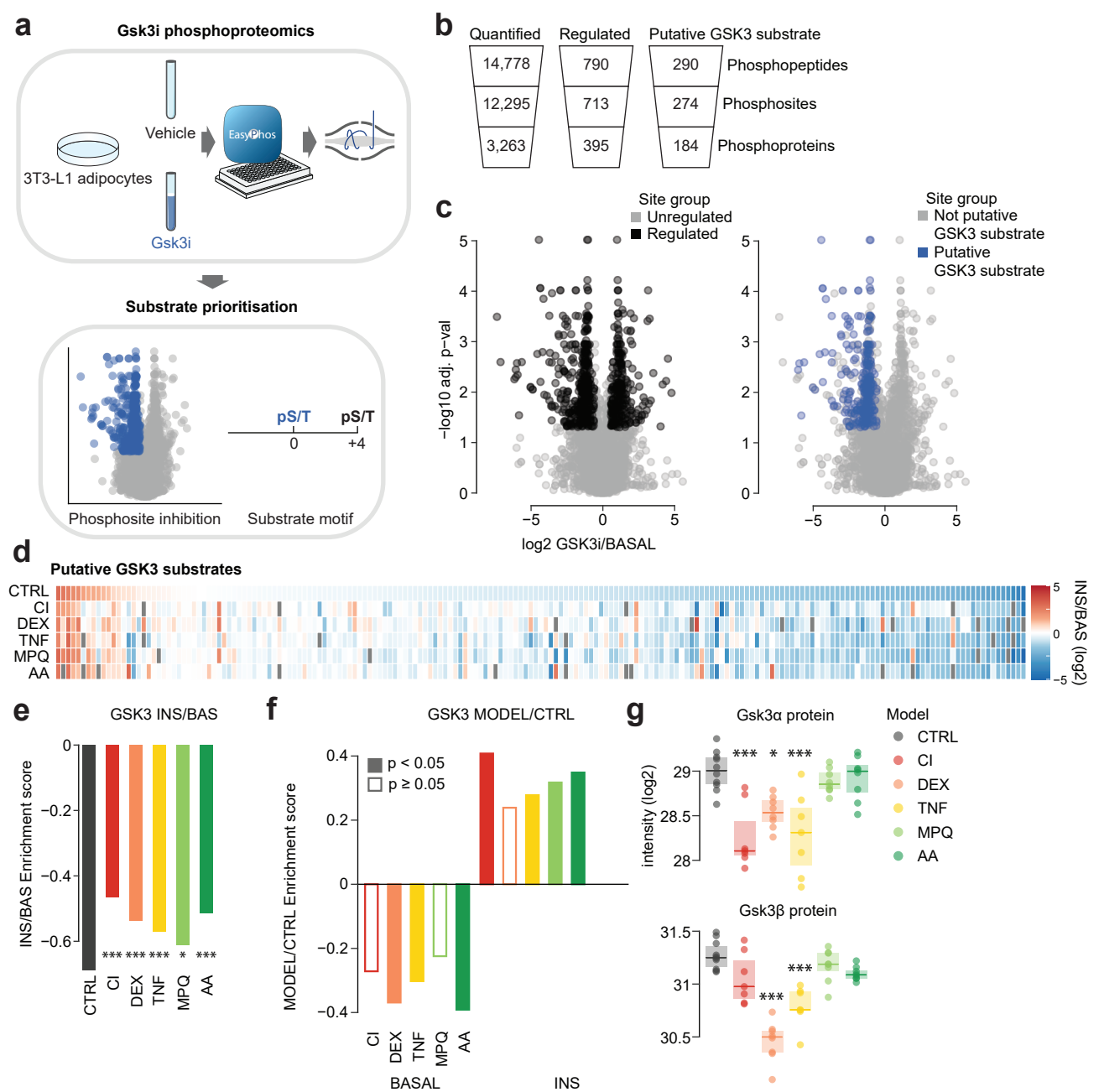
a
Gsk3i phosphoproteomics
Vehicle
3T3-L1 adipocytes
Gsk3i
EasyPhos
Substrate prioritisation
pS/T
pS/T
0
+4
Phosphosite inhibition
Substrate motif
b
Quantified
Regulated
Putative GSK3 substrate
14,778
790
290
Phosphopeptides
12,295
713
274
Phosphosites
3,263
395
184
Phosphoproteins
c
Site group
Unregulated
Regulated
Site group
Not putative GSK3 substrate
Putative GSK3 substrate
−log10 adj. p−val
log2 GSK3i/BASAL
d
Putative GSK3 substrates
CTRL
CI
DEX
TNF
MPQ
AA
INS/BAS (log2)
e
GSK3 INS/BAS
INS/BAS Enrichment score
f
GSK3 MODEL/CTRL
p < 0.05
p ≥ 0.05
MODEL/CTRL Enrichment score
BASAL
INS
g
Gsk3α protein
Gsk3β protein
intensity (log2)
Model
CTRL
CI
DEX
TNF
MPQ
AA

***Fig 3: Insulin-regulated inhibition of the kinase GSK3 is impaired in insulin resistance***

(**A**) Pipeline for identification of context-specific kinase substrates, exemplified by GSK3 in 3T3-L1 adipocytes. (**B**) Quantification from GSK3 inhibitor phosphoproteomics. (**C**) The effect of GSK3 inhibition on the 3T3-L1 adipocyte phosphoproteome. Black indicates phosphopeptides regulated by GSK3 inhibition and blue indicates down-regulated phosphopeptides matching the GSK3 substrate motif. (**D**) Putative GSK3 substrates quantified in 3T3-L1 insulin resistance phosphoproteome. Only phosphopeptides quantified in BAS and INS in at least four models are shown, and missing values are colored gray. (**E**) KSEA in each insulin resistance model using log2 INS/BAS fold changes and putative GSK3 substrates decreased in CTRL cells (log2 INS/BAS < 0). To examine differences between control cells and models, KSEA was performed using log2 INS/BAS fold changes normalized to control cells (*). (**F**) KSEA in unstimulated (BASAL) and insulin-stimulated (INS) phosphoproteomes using log2 Model/CTRL fold changes and the same substrates as in (**E**). Filled-in columns indicate significant changes in GSK3 activity. (**G**) Intensity of GSK3α/β total protein with significant differences compared to control cells indicated (*). *: $0.01 < p < 0.05$, **: $0.001 < p < 0.01$, ***: $p < 0.001$ (ANOVA, Dunnett's post hoc tests).

***Insulin-regulated inhibition of the kinase GSK3 is impaired in insulin resistance***

To utilize this adipocyte-specific GSK3 substrate data to analyze our insulin signaling data, we next mapped the 274 putative GSK3 substrate phosphosites onto our 3T3-L1 insulin resistance phosphoproteome data. We found high overlap between these datasets, identifying 191 corresponding phosphosites that decreased in abundance in response to insulin ($\log_2$ insulin/basal < 0), further supporting that these sites were regulated by GSK3 in adipocytes. Performing a KSEA using these sites revealed that GSK3 was inactivated in response to insulin in control cells in our original phosphoproteomics study, and remarkably, that this inactivation was attenuated across all insulin resistance models (**Fig. 3D, E**). Putative GSK3 substrates with defective dephosphorylation in insulin resistance included S520 and S553 on PHLDB1; S350, S354, and S358 on the microtubule regulator SLAIN2; and S1036 on ASK1 (**Fig. S4H**). Of note, the ASK1 inhibitory site S1040 is the priming site for S1036, and both sites display defective dephosphorylation in four 3T3-L1 models (**Fig. 2F**). These sites therefore represent an unappreciated intersection between GSK3 and ASK1 signaling that is altered in insulin resistance. In addition, the GLUT4 translocation-regulator PHLDB1 contained a site that was emergent in 4 models (**Fig. 2G**), marking PHLDB1 as a node of crosstalk for signaling pathways both attenuated and promoted in insulin resistance. Our context-specific kinase substrate profiling suggests that the deactivation of GSK3 by insulin is impaired in multiple models of insulin resistance, and that this may contribute to the impaired protein dephosphorylation, and defective insulin-stimulated glucose transport, observed across these models.

Impaired insulin-stimulated GSK3 deactivation could be driven by lower unstimulated activity or elevated insulin-stimulated activity, or both. To distinguish these possibilities, we performed KSEA on phosphopeptide abundance relative to control cells, under both unstimulated and insulin-stimulated conditions. In unstimulated cells, DEX, TNF and AA had reduced GSK3 activity relative to control, while in insulin-stimulated cells, CI, TNF, MPQ and AA had

increased GSK3 activity relative to control (**Fig. 3F**). Overall, more models had altered GSK3 activity in the insulin-stimulated state, suggesting that the primary defect of GSK3 regulation in insulin resistance is the inability of insulin to attenuate GSK3 activity.

We next asked whether changes in the abundance of GSK3α and GSK3β isoforms and/or inhibitory phosphorylation of GSK3 by AKT could explain the observed changes in GSK3 activity. GSK3 protein expression was decreased in most chronic 3T3-L1 models (**Fig. 3G**; GSK3α; CI, DEX, and TNF; GSK3β (DEX, TNF). However, the same changes were not observed in acute models (MPQ, AA), despite impaired insulin-dependent GSK3 signaling (**Fig. 3G**). In some cases, impaired GSK3 activity may be partially driven by impaired phosphorylation of the AKT inhibitory sites, as insulin-mediated phosphorylation of GSK3α S21 was attenuated in CI and TNF models, as was insulin-mediated GSK3β S9 phosphorylation in CI, DEX, and TNF (**Fig. 2B**). However, normalizing phosphorylated GSK3 to the total protein abundance suggested that these changes in S21 or S9 phosphorylation in DEX and TNF could potentially be explained by decreased expression of GSK3, while the changes in CI were additionally mediated by decreased AKT signaling to GSK3 (**Fig. S4I**). Notably, as inhibitory phosphorylation and protein abundance were decreased to a similar extent in TNF, inhibitory phosphorylation should not explain why insulin-stimulated GSK3 activity was increased in TNF relative to control. Although these alterations in protein expression and signaling to GSK3 may, to some extent, explain the behavior of GSK3 in our chronic models (CI, DEX, and TNF), they do not explain the impairment in GSK3 inactivation observed in our acute models (MPQ, AA) (summarized in **Table 1**). This suggests that aside from protein abundance and insulin signaling to GSK3, other factors that control GSK3 are likely dysregulated in insulin resistance.

***Signaling rewiring and GSK3 dysregulation in insulin resistant adipose tissue***

We next assessed if key findings from 3T3-L1 adipocytes, including impaired GSK3 regulation, were recapitulated in *in vivo* models of insulin resistance. To this end, we fed mice either a chow diet (**CHOW**) or a high fat high sucrose diet (HFD) for 14 d (insulin-resistant

(**HFD**))[3]. For a third group of mice fed HFD for 14 d, we switched the diet back to chow for a further 5 d (reversal of insulin resistance (**REV**), **Fig. 4A**). In the mice fed a 14 d HFD, insulin-stimulated 2DG into epididymal adipose tissue was reduced compared to the CHOW group, while returning mice to a chow diet for 5 days improved insulin sensitivity by approximately 40% (**Fig. 4B**).

To assess insulin signaling we performed phosphoproteomic analysis of epididymal adipose tissue from CHOW, HFD and REV mice treated with saline or insulin (**Fig. 4C, S5A-D**). We identified 319 insulin-regulated phosphopeptides on 210 proteins in CHOW mice (**Fig. 4C, Data S6**). Insulin signaling was substantially rewired in HFD mice, as 203 of these 319 phosphopeptides were no longer insulin-responsive in HFD, while a separate set of 105 phosphopeptides displayed emergent insulin-regulation in HFD (**Fig. 4D, S5E Data S6**). Akin to insulin-resistant 3T3-L1 adipocytes, the majority of the 203 defective phosphopeptides were outside core insulin signaling pathways (**Fig. 4E**), and emergent phosphorylation was enriched in transcriptional regulators (**Fig. S5F**). We next assessed whether GSK3 activity was altered in insulin resistant adipose tissue, using our adipocyte-specific list of GSK3 substrates. KSEA on the 168 GSK3 substrates downregulated by insulin in CHOW tissue (CHOW $\log_2$ fold-change < 0) revealed that insulin-stimulated GSK3 deactivation was impaired in HFD and partially restored in REV tissue (**Fig. 4F**). As adipose tissue insulin sensitivity was also impaired in HFD and partially restored in REV (**Fig. 4B**), this supports the notion that insulin regulation of GSK3 is important for insulin sensitivity. GSK3 substrates with defective dephosphorylation in HFD tissue included S72 on TRARG1 (**Fig. S5G**). Trarg1 has been implicated in GLUT4 trafficking[54,55], and the dephosphorylation of this site may promote GLUT4 translocation[56], so Trarg1 may link GSK3 dysregulation to impaired GLUT4 trafficking in insulin resistance.

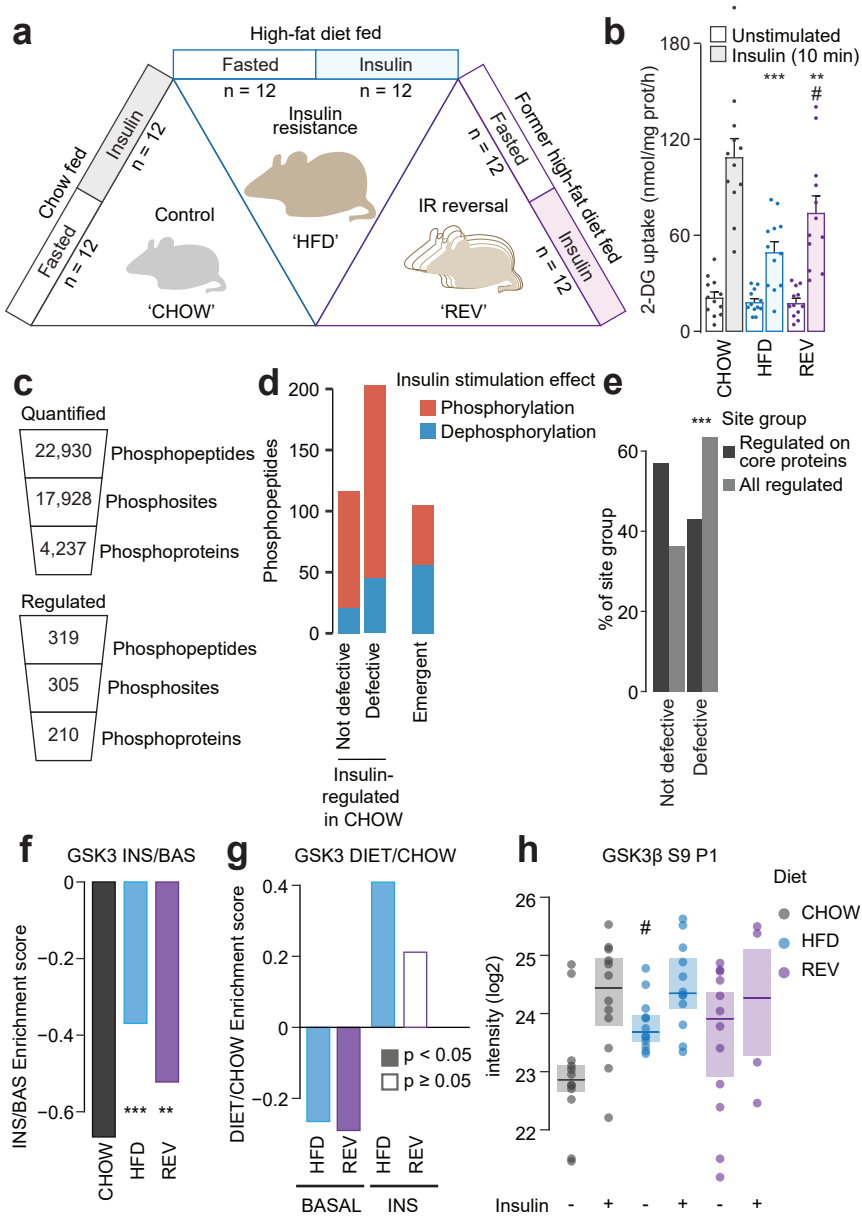
a
High-fat diet fed
Fasted
Insulin
n = 12
n = 12
Insulin resistance
'HFD'
Chow fed
Insulin
n = 12
Fasted
n = 12
Control
'CHOW'
Former high-fat diet fed
Fasted
n = 12
Insulin
n = 12
IR reversal
'REV'
b
Unstimulated
Insulin (10 min)
2-DG uptake (nmol/mg prot/h)
180
120
60
0
***
**
#
CHOW
HFD
REV
c
Quantified
22,930
Phosphopeptides
17,928
Phosphosites
4,237
Phosphoproteins
Regulated
319
Phosphopeptides
305
Phosphosites
210
Phosphoproteins
d
Insulin stimulation effect
Phosphorylation
Dephosphorylation
Phosphopeptides
200
150
100
50
0
Not defective
Defective
Emergent
Insulin-regulated in CHOW
e
*** Site group
Regulated on core proteins
All regulated
% of site group
60
40
20
0
Not defective
Defective
f
GSK3 INS/BAS
INS/BAS Enrichment score
0
−0.2
−0.4
−0.6
***
**
CHOW
HFD
REV
g
GSK3 DIET/CHOW
DIET/CHOW Enrichment score
0.4
0.2
0
−0.2
p < 0.05
p ≥ 0.05
HFD
REV
HFD
REV
BASAL
INS
h
GSK3β S9 P1
Diet
CHOW
HFD
REV
intensity (log2)
26
25
24
23
22
#
Insulin
-
+
-
+
-
+

***Fig 4: Impaired inhibition of GSK3 in insulin resistant adipose tissue***

(**A**) Diet regimes and sample sizes for phosphoproteomic analysis of adipose tissue. (**B**) $^{3}$H-2DG uptake into epididymal adipose tissue during 10 min intraperitoneal injection with insulin or saline. Data were analyzed by two-way ANOVA corrected for multiple comparisons (Tukey's test) to compare between CHOW and HFD or REV groups (*), and HFD and REV groups (#). Error bars are S.E.M. n = 12. (**C**) Quantification from phosphoproteomic analysis of adipose tissue. (**D**) The number of phosphopeptides that were significantly regulated by insulin in CHOW mice, further divided into sites that were defective in HFD mice. The number of phosphopeptides emergent in HFD is also shown. (**E**) The distribution of phosphorylation defects among regulated phosphopeptides on all proteins or proteins considered part of the core insulin signaling pathway. A one-sided Fisher's exact test was performed to assess whether regulated phosphopeptides on core insulin signaling protein were less likely to be defective than expected by chance (*). (**F**) KSEA was performed using log2 INS/BAS fold changes and putative GSK3 substrates that were decreased in CHOW mice (log2 INS/BAS < 0). KSEA was performed using log2 INS/BAS fold changes in HFD and REV normalized to CHOW to assess differences between diets (*). (**G**) KSEA was performed in the unstimulated (BASAL) and insulin-stimulated (INS) phosphoproteomes using log2 DIET/CHOW fold changes and the same substrates as in (**F**). Filled-in columns indicate significant changes in GSK3 activity. (**H**) Intensity of GSK3β S9. t-tests were performed to compare HFD or REV to CHOW in unstimulated (#) or insulin-stimulated (*) mice. *: $0.01 < p < 0.05$, **: $0.001 < p < 0.01$, ***: $p < 0.001$.

As in 3T3-L1 adipocyte models of insulin resistance, the dysregulation of GSK3 in insulin resistant tissue was due to a combination of altered activity before and after insulin stimulation (**Fig. 4G**). In particular, before insulin stimulation, GSK3 activity was decreased in HFD and REV tissue compared to CHOW (**Fig. 4G**), which may be due to increased inhibitory phosphorylation of S9 on GSK3β (**Fig. 4H**). Phosphorylation of S21 on GSK3α was not adequately quantified. After insulin stimulation GSK3 activity was elevated in HFD (**Fig. 4G**), however this cannot be explained by S9 phosphorylation as this was equivalent to that observed in adipose tissue from CHOW fed mice (**Fig. 4H**). In addition, these changes in GSK3 activity were more pronounced in insulin-stimulated tissue compared to unstimulated tissue, supporting the observation we made in 3T3-L1 adipocytes that GSK3 dysregulation is mainly due to the inability of insulin to lower its activity. Collectively, phosphoproteomic analysis of *in vivo* models of insulin resistance recapitulated key findings from 3T3-L1 adipocytes, including the observation that regulation of GSK3 by insulin is impaired in insulin resistance (**Table 1**).

| | | CI | DEX | TNF | MPQ | AA | HFD | REV |
|---|---|---|---|---|---|---|---|---|
| ***GSK3 KSEA*** | **Magnitude of insulin response** | ↓ | ↓ | ↓ | ↓ | ↓ | ↓ | ↓ |
| | **Unstimulated activity** | | ↓ | ↓ | | ↓ | ↓ | ↓ |
| | **Insulin-stimulated activity** | ↑ | | ↑ | ↑ | ↑ | ↑ | |
| ***GSK3b*** | **Protein** | | ↓ | ↓ | | | NA | NA |
| | **Unstimulated pS9** | | ↓ | ↓ | | | ↑ | |
| | **Insulin-stimulated pS9** | ↓ | ↓ | ↓ | | | | |
| | **Insulin-stimulated pS9 normalized to protein** | | | | | | NA | NA |
| ***GSK3a*** | **Protein** | ↓ | ↓ | ↓ | | | NA | NA |
| | **Unstimulated pS21** | | | ↓ | | | NA | NA |
| | **Insulin-stimulated pS21** | ↓ | | ↓ | | | NA | NA |
| | **Insulin-stimulated pS21 normalized to protein** | ↓ | | | | | NA | NA |

***Table 1: GSK3 changes in insulin resistance***
Statistically significant changes in GSK3 activity (estimated by KSEA), protein abundance, and inhibitory phosphorylation relative to CTRL or CHOW. Blank cells indicate no significant change. Adipose tissue total protein was not measured and GSK3a S21 was poorly quantified, so the relevant cells are marked NA.

***Pharmacological inhibition of GSK3 rescues insulin resistance in vitro and ex vivo***

In our analysis of 3T3-L1 models of adipocyte insulin resistance we detected multiple insulin signaling alterations shared across different models, leading us to hypothesize that pharmacological targeting of any one of these alterations may only confer a partial reversal of insulin resistance. As impaired deactivation of GSK3 by insulin was observed in all insulin resistant 3T3-L1 models and insulin resistant adipose tissue, we decided to test this hypothesis on GSK3. We treated insulin-resistant 3T3-L1 adipocytes (CI, DEX, and TNF) with GSK3i or another GSK3 inhibitor CHIR99021 (CHIR) 1.5 h prior to administration of insulin, and monitored plasma membrane GLUT4 using an antibody that recognizes an exofacial region of GLUT4[57], or by stably expressing an HA-GLUT4-mRuby3 reporter construct. All three insulin resistance treatments impaired insulin-stimulated GLUT4 translocation in response to 0.5 or 100 nM insulin in wild type or HA-GLUT4-mRuby3-expressing cells (**Fig. 5A, C**). GSK3 inhibition increased cell surface endogenous GLUT4 and HA-GLUT4-mRuby3 in control, TNF and DEX-treated cells. The response to GSK3 inhibition was much greater in TNF and DEX models than in control cells (**Fig. 5B, D**) so that, except for DEX-treated wild type cells, insulin responses were nearly equivalent to control cells. However, CI-treated cells were largely refractory to GSK3 inhibition (**Fig. 5A-D**). Notably, the effects of these GSK3 inhibitors in the DEX and TNF models were only observed in insulin-stimulated cells, suggesting that this intervention acts by specifically augmenting the insulin response.

We also examined the effect of GSK3i in explants derived from insulin-sensitive (CHOW) and insulin-resistant (HFD) mouse adipose tissue. Insulin-stimulated 2DG uptake was reduced in control DMSO-treated explants from HFD-fed mice at both 0.5 and 10 nM insulin, confirming that they were insulin resistant (**Fig. 5E**). Crucially, 1 hour pretreatment with GSK3i increased insulin-stimulated 2DG uptake at a submaximal insulin concentration (0.5 nM) in explants from HFD-fed mice (**Fig. 5E**). This effect was not observed in these explants at 10 nM insulin, nor in explants from chow-fed mice at either insulin concentration.

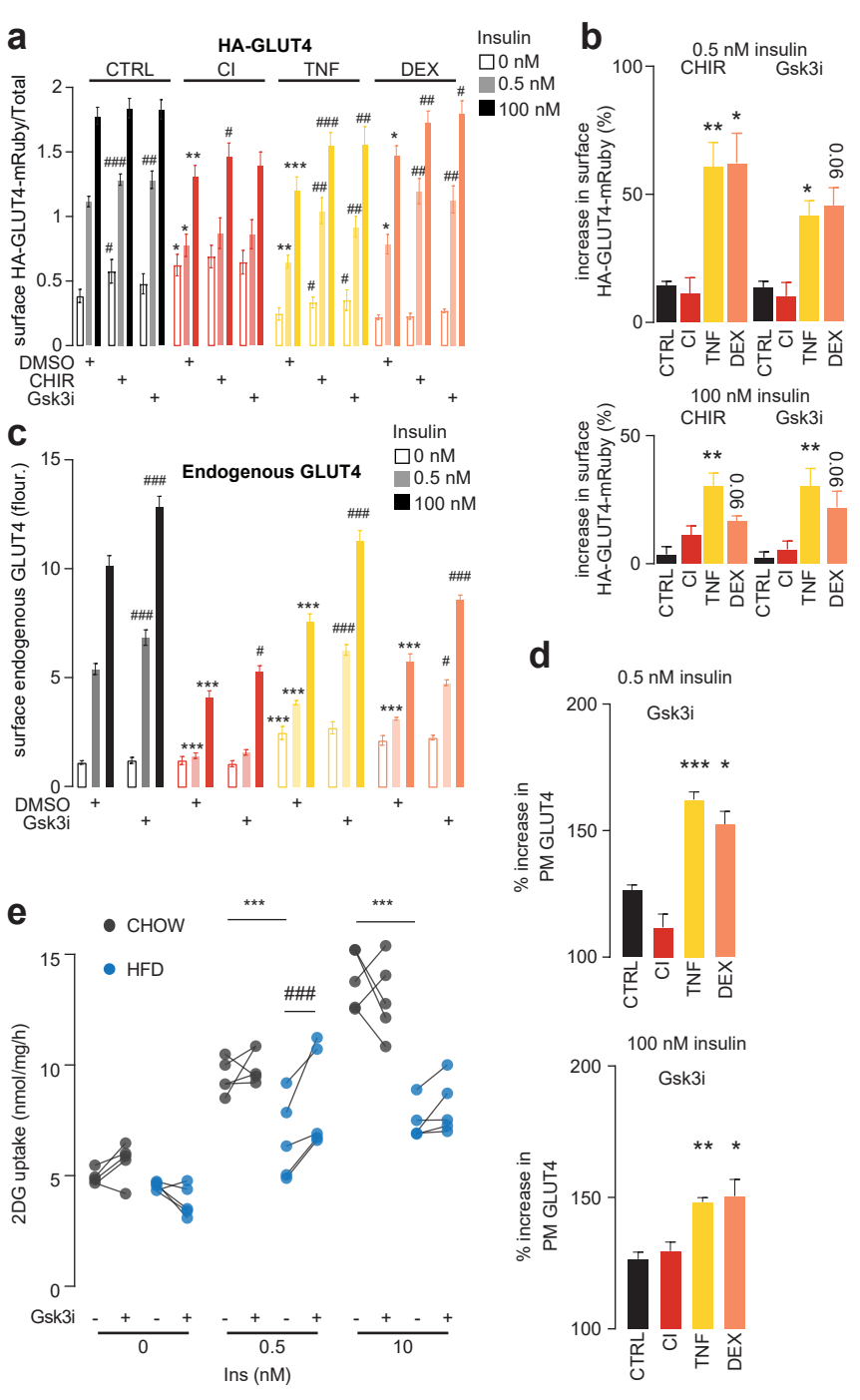
a
HA-GLUT4
CTRL
CI
TNF
DEX
Insulin
0 nM
0.5 nM
100 nM
surface HA-GLUT4-mRuby/Total
DMSO
CHIR
Gsk3i
b
0.5 nM insulin
CHIR
Gsk3i
increase in surface HA-GLUT4-mRuby (%)
90'0
100 nM insulin
c
Endogenous GLUT4
surface endogenous GLUT4 (flour.)
d
0.5 nM insulin
Gsk3i
% increase in PM GLUT4
100 nM insulin
e
CHOW
HFD
2DG uptake (nmol/mg/h)
Ins (nM)

***Fig 5: Pharmacological inhibition of GSK3 rescues insulin resistance in vitro and ex vivo***

(**A**) Control and insulin resistant 3T3-L1 adipocytes expressing HA-GLUT4-mRuby3 were pretreated for 90 min with DMSO or a GSK3 inhibitor (10 μM CHIR99021, "CHIR"; or 500 nM LY2090314, "GSK3i"), following a 20 min insulin treatment. The normalized abundance of HA-GLUT4-mRuby3 at the plasma membrane was compared between control and insulin resistant cells treated with DMSO (*), and between CHIR/GSK3i-treated cells and DMSO-treated cells within each insulin resistance model (#), using two-way ANOVAs and Dunnett's post-hoc tests. Error bars are S.E.M., n = 5-7. (**B**) The percentage increase in PM HA-GLUT4 caused by GSK3 inhibition at 0.5 nM or 100 nM insulin. Data were analyzed by mixed-effects analysis corrected for multiple comparisons (Dunnett's test), comparing control vs insulin resistant models (*). Error bars are S.E.M., n = 5-7. (**C**) Control and insulin resistance wild-type 3T3-L1 adipocytes were pretreated for 90 min with DMSO or a 500 nM LY2090314 (GSK3i) following a 20 min insulin treatment. The plasma membrane abundance of GLUT4 was analyzed as in (**A**). Error bars are S.E.M., n = 8 for CTRL, CI and TNF, 4 for DEX. (**D**) Percentage increase in PM GLUT4 caused by GSK3 inhibition at 0.5 nM or 100 nM insulin, analyzed as in (**B**) (*). Error bars are S.E.M., n = 8 for CTRL, CI and TNF, 4 for DEX. (**E**) Epididymal fat explants from mice fed CHOW or HFD for 14 d were pretreated with either DMSO or 500 nM LY2090314 (GSK3i) for 60 min. $^{3}$H-2DG uptake was assessed during a 20 min insulin stimulation. HFD was compared to CHOW in DMSO-treated explants (*), and DMSO-treated explants were compared to GSK3i-treated explants in either HFD or CHOW (#), using two-way repeated-measures ANOVAs followed by Šídák's post-hoc tests. Lines connect data points from the same mouse. n = 5. *: $0.01 < p < 0.05$, **: $0.001 < p < 0.01$, ***: $p < 0.001$.

Previous studies have found acute and chronic inhibition of GSK3 in rodent models of insulin resistance improved insulin-stimulated glucose uptake into muscle[58–61]. Our results complement this body of research indicating that acute inhibition of GSK3 can ameliorate adipocyte insulin resistance in diverse contexts. The reversal of insulin resistance provided by GSK3 inhibition was only partial, lending evidence to our hypothesis that insulin resistance is driven by multiple, cumulative signaling derangements.

## Discussion

Here we employed state-of-the-art phosphoproteomics to interrogate signaling networks in insulin resistant adipocytes. This is highly relevant to metabolic disease in humans as adipose insulin resistance is an early event in the path to type 2 diabetes, and disrupting insulin-stimulated glucose uptake in adipocytes compromises whole-body glucose homeostasis[4,5]. Previous targeted studies have associated insulin resistance with defects in proximal insulin signaling proteins, including AKT, IRS1/2, and the insulin receptor. However, the relevance of these findings has been challenged[1,16], calling for more global, untargeted analyses of signaling in insulin resistance. Here we address this for the first time in adipocytes. By utilizing standardized and controlled cell culture models spanning a wide range of known contributors to insulin resistance, we observed that insulin resistance involves a profound rewiring of many nodes within the insulin signaling network. Pharmacologically targeting one of these nodes in isolation improved insulin sensitivity, but only partially. This highlights the utility of our approach in identifying targets to ameliorate metabolic dysfunction, and also supports the concept that insulin resistance is a complex multi-nodal defect. Correction of this defect will either require identification of common regulators of these discrete nodes or treatments designed to target multiple nodes. We verified these observations in adipose tissue from mice fed different diets, supporting the physiological relevance of our findings.

Despite substantial rewiring of insulin signaling across insulin resistance models, the regulation of canonical insulin-responsive kinases and phosphoproteins was overwhelmingly unchanged. To gain a deeper understanding of insulin resistance it is therefore necessary to venture into the vast, non-canonical regions of insulin signaling. However, as is the case for the majority of identified phosphosites[62], most dysregulated phosphosites lacked an annotated upstream kinase and have not been functionally characterized. We therefore have little means of rationalizing how these phosphosites might be dysregulated in insulin resistance, or how they might contribute to the insulin resistance phenotype. Recent *in vitro* approaches have begun to address one of these hurdles by systematically identifying thousands of kinase-phosphosite relationships[63]. *In vivo* methods using kinase inhibitors are likely to yield additional insights as they retain the stoichiometry and subcellular context of the proteome. In line with this view, we employed a pipeline for identifying context-specific kinase substrates that identified hundreds of putative GSK3 substrates in adipocytes, and these data subsequently facilitated the detection of GSK3 dysregulation whereas existing annotations could not. Beyond mapping upstream regulators of phosphosites, recent computational[64] and biochemical[65] approaches have made progress in estimating whether a given phosphosite will have a downstream regulatory role, though they are yet to tailor predictions to different experimental contexts. Sustained efforts to map signaling topology and function will reveal how the signaling alterations we identified in insulin resistance are imbedded within and shape the insulin signaling network.

Kinases are popular targets for drug discovery efforts[66], and, as we have presented for GSK3, mapping upstream regulators of dysregulated phosphosites will identify kinases that could be pharmacologically targeted to ameliorate insulin resistance. Interestingly, there is also evidence that GSK3 hyperactivation drives dysfunction of the diabetic islet[67] and that GSK3 hyperactivation in the hypothalamus impairs glucose homeostasis[68]. Hence, targeting GSK3 could provide a route to combating multi-organ dysfunction in the progression to type 2

diabetes. An alternative strategy for treating insulin resistance is to target molecular factors upstream of multiple phosphorylation defects. Reactive oxygen species (ROS) are elevated in all models we studied[3,22,23]. In contrast to GSK3 inhibition, quenching of ROS more completely reversed insulin resistance in our models[22], suggesting that ROS may dysregulate insulin signaling at several distinct nodes. In support of this concept, ROS can crosstalk with phosphorylation through protein redox modification[69]. For example, ROS can deactivate phosphatases including PP1[70], which may play a role in the preferential defect in insulin-stimulated dephosphorylation we observed. Moreover, GSK3β is oxidized at the functionally uncharacterized residues Cys107 and Cys76 in adipocytes following oxidative stress[69]. As protein abundance and inhibitory phosphorylation could only partially explain the changes in GSK3 activity observed in insulin resistance, redox modifications may also be involved. To clarify and expand on these possibilities, future work should globally dissect the crosstalk between protein redox modification and phosphorylation in insulin resistance.

Here we provide a global view of the signaling rearrangements that occur during adipocyte insulin resistance and augment these data with an approach to chart dysregulated kinase signaling in a context-specific manner. Our data suggest insulin resistance may arise from the cumulative contributions of diverse signaling derangements, and we highlight many such putative mediators that warrant further investigation.

**Acknowledgements**

This work was supported by National Health and Medical Research Council (NHMRC) Project Grant GNT1120201 and GNT1061122 (to D.E.J.). D.E.J. is an Australian Research Council (ARC) Laureate Fellow. The content is solely the responsibility of the authors and does not necessarily represent the official views of the NHMRC or ARC. The authors acknowledge the facilities, and the scientific and technical assistance of the Sydney Mass Spectrometry Facility, the Sydney Preclinical Imaging Facility and the Laboratory Animal Services at the Charles Perkins Centre, University of Sydney. D.J.F. was supported by a Medical Research Council

Career Development Award (MR/S007091/1) and a Wellcome Institution Strategic Support Fund award (204845/Z/16/Z). These studies were supported by the Wellcome-MRC, Institute of Metabolic Science, Metabolic Research Laboratories, Imaging Core (Wellcome Trust Major Award [208363/Z/17/Z]).

## Author Contributions

Conceptualization: DJF, PY, DEJ, SJH. Investigation: DJF, JvG, KCC, XD, SM, DMN, ASS, JRK, MRW, JTB, SJH. Methodology: DJF, JvG, KCC, JRK, JGB, SJH. Formal analysis: DJF, JvG, EJN, PY, SJH. Visualization: DJF, JvG, SJH. Software: JvG, SJH. Resources: DJF, MRW, JTB, DEJ. Project administration: DJF, JvG, SJH. Funding acquisition: DJF, DEJ. Supervision: DJF, EJN, DEJ, SJH. Writing- original draft: DJF, JvG, DEJ, SJH. Writing-review and editing: All authors

## Competing Interests

The authors state that they have potential conflicts of interest regarding this work: MRW and JTB were employees of Eli Lilly during the study.

## Materials and Correspondence

Correspondence: sean.humphrey@sydney.edu.au, david.james@sydney.edu.au, djf72@medschl.cam.ac.uk

## Data Availability Statement

All raw and MaxQuant processed phosphoproteomics data have been deposited in the PRIDE proteomeXchange repository and will be made accessible upon publication or immediately on request. Processed data be explored online at www.adipocyteatlas.org and will be made available as supplementary tables upon publication or immediately on request.

## Code Availability Statement

All code used to analyze data and produce figures is available on request and will be made publicly available upon publication.

## Rights Retention Statement

This work was funded by a UKRI grant (MR/S007091/1). For the purpose of open access, the author has applied a Creative Commons Attribution (CC BY) licence to any Author Accepted Manuscript version arising.

## Methods

### *3T3-L1 fibroblast culture and differentiation into adipocytes*

Mycoplasma-free 3T3-L1 fibroblasts were obtained from 3T3-L1 Howard Green (Harvard Medical School, Boston, MA) were maintained in Dulbecco's Modified Eagle Medium (DMEM) (Thermo Fisher Scientific) supplemented with 10% fetal calf serum (FCS) (Thermo Fisher Scientific) and 1% GlutaMAX (Thermo Fisher Scientific) in a humidified atmosphere with 10% $CO_2$. HA-GLUT4 overexpressing cell lines were generated by retroviral transduction of 3T3-L1 fibroblasts as previously described [71]. Confluent 3T3-L1 cells were differentiated into adipocytes by addition of DMEM/10% FCS/GlutaMAX containing 0.22 µM dexamethasone, 100 ng/mL biotin, 2 µg/mL insulin, 500 µM IBMX (day 0). After 72 h, medium was replaced with DMEM/10% FCS/GlutaMAX containing 2 µg/mL insulin (day three post differentiation). After a further 72 h (day six post differentiation), cells were switched to DMEM/10% FCS/GlutaMAX. Medium was subsequently replaced every 48 h. Cells were used between days 10 and 15 after the initiation of differentiation

### *In vitro models of insulin resistance*

Insulin resistance was induced by hyperinsulinemia, dexamethasone, tumor necrosis factor-α (TNF), antimycin A or mitoParaquat (MPQ) as previously described [3,22,23,72].The chronic insulin (**CI**) model of hyperinsulinemia was created by incubation of adipocytes with 10 nM insulin for 24 h (add insulin at 1200, 1600 and 2000 h on day 1 and 0800 h the following day, prior to serum starvation at 1200 on day 2). Glucocorticoid-induced insulin resistance was recreated with 20 nM dexamethasone (**Dex**) (0.01% ethanol carrier as control), starting on day seven post initiation of differentiation and maintained for 8 d. Medium was changed every 48 h. Chronic low-dose inflammation was mimicked in 3T3-L1 adipocytes by incubation with 2 ng/mL TNFα (**TNF**; Calbiochem) for 4 d. Medium was changed every 24 h. Following CI, Dex of TNF treatment, cells were washed and serum-starved for 1.5 h in the absence of insulin, dexamethasone or TNFα prior to insulin stimulation. Mitochondrial oxidants were induced by incubation with 50 nM antimycin A or 25 µM mPQ for 1.5 h during serum starvation. Note that 25 µM mPQ was used in this study as all samples for phosphoproteomic analysis were undertaken in day 15 adipocytes, and this dose was required for sufficient induction of mitochondrial oxidants and insulin resistance in these cells.

***3T3-L1 adipocyte treatment (insulin and GSK3i)***

For acute insulin and GSK3i treatments, 3T3-L1 adipocytes were used at 10 days post-differentiation, and serum starved for 2 h prior to treatments. For insulin treatments, cells were serum-starved prior to treatment with DMSO or the GSK3 inhibitor LY2090314 at 100 nM, for 20 min. Cells were then washed three times with ice-cold TBS before scraping in SDC lysis buffer (4% Sodium Deoxycholate, 100 mM Tris pH 8.5) with heating for 5 min at 95 °C. Lysates were sonicated (75% output power, 2x 30 s) and centrifuged for 20 min at 20,000 xg at 0 °C to form a lipid layer. Clarified protein lysate was carefully collected without interfering with the upper lipid layer, and protein concentration was measured using BCA assay.

***Phosphoproteomics sample preparation***

240 µg protein was reduced and alkylated in one step using 10 mM Tris (2-carboxyethyl)phosphine (TCEP) and 40 mM 2-Chloroacetamide (CAA) at 45 °C for 5 minutes. LysC and trypsin (1:100 enzyme-protein ratio) were added to samples to digest the protein in a 96-well plate at 37 °C overnight. 1:6 of the peptides (40 µg) were taken for proteome analysis, and for the remaining phosphopeptides were enriched according to the EasyPhos method (Humphrey, Karayel, James, & Mann, 2018). Phosphopeptides were resuspended in 5 µl MS loading buffer (2% ACN, 0.3% TFA) for LC-MS/MS analysis.

***Proteome sample preparation***

40 µg peptides were fractionated by offline Strong Cation Exchange using SCX StageTips as described [73]. Briefly, StageTips fabricated with 6-layers of SCX material (3M Empore) were equilibrated sequentially: 1x 100 µL ACN, 1x 100 µL 30% MeOH/1% TFA, 1x 100 µL 0.2% TFA, and de-salted peptides were loaded onto StageTips in 100 µL 1% TFA. Peptides were sequentially eluted with 6 elution buffers of increasing strength as follows: (1) 50 mM $NH_4OAc$/20% ACN/0.5% Formic acid; (2) 75 mM $NH_4OAc$/20% ACN/0.5% Formic acid; (3) 125 mM $NH_4OAc$/20% ACN/0.5% Formic acid; (4) 200 mM $NH_4OAc$/20% ACN/0.5% Formic acid; (5) 300 mM $NH_4OAc$/20% ACN/0.5% Formic acid; (6) 5% ammonium hydroxide/80% ACN. Fractions were collected separately, and dried in a vacuum concentrator (Eppendorf). Peptides were resuspended in MS loading buffer (2% ACN, 0.3% TFA) for LC-MS/MS analysis.

***Liquid chromatography-tandem mass spectrometry (LC-MS/MS)***

*DIA-MS (3T3-L1 phosphoproteomes):* peptides were loaded onto in-house fabricated 50 cm columns with a 75-µM I.D., packed with 1.9 µM C18 ReproSil Pur AQ particles using a Dionex U3000 HPLC coupled to an Orbitrap Exploris 480 mass spectrometer (Thermo Fisher Scientific). Column temperature was maintained at 60°C with a Sonation column oven, and peptides separated using a binary buffer system comprising 0.1% formic acid (buffer A) and 80% ACN plus 0.1% formic (buffer B), at a flow rate of 400 nl/min, with a gradient of 3–19% buffer B over 80 min followed by 19–41% buffer B over 40 min, resulting in ~2-h gradients. Peptides were analyzed with one full scan (350–1,400 m/z, R = 120,000) at a target of 3e6 ions, followed by 48 data-independent acquisition (DIA) MS/MS scans (350–1,022 m/z) with higher-energy collisional dissociation (HCD) (target $3e^6$ ions, max injection time 22 ms, isolation window 14 m/z, 1 m/z window overlap, normalized collision energy (NCE) 25%), with fragments detected in the Orbitrap (R = 15,000).

*DDA-MS (3T3-L1 proteomes):* Peptides were loaded onto 50 cm fused silica columns packed in-house (ReproSil Pur C18-AQ, 1.9 µm particle size) and maintained at 60 °C using a column oven (Sonation, GmbH). Peptides were separated by reversed-phase chromatography using an Easy nLC 1200 (Thermo Fisher Scientific), with a binary buffer system of 0.1% formic acid (buffer A) and 80% ACN/0.1% formic (buffer B). Peptides were separated by linear gradients of buffer B (3% to 25% over 90 min, followed by 25-35% over 20 min, and 35-60% over 10 min) at a flow rate of 300 nL/min, and electrosprayed directly into the mass spectrometer by the application of 2.4 kV with a liquid junction union. Ionized peptides were analyzed using a benchtop Orbitrap (Q Exactive HF-X) mass spectrometer (Thermo Fisher Scientific). The mass spectrometer was operated in data-dependent mode, performing survey scans of $3e^6$ ions at a resolution of 60,000 from 300-1,650 m/z. The 15 most abundant precursors from the survey scan with charge state >1 and <5 were selected for fragmentation. Precursors were isolated with a window of 1.4 m/z and fragmented in the HCD cell with NCE of 27. Maximum ion fill times for the MS/MS scans were 28 ms, with a target of $2.9e^3$ ions (intensity threshold $2.9e^5$ ions). Fragment ions were analyzed with high resolution (15,000) in the Orbitrap mass analyzer. Dynamic exclusion was enabled with duration 30s.

*DDA-MS (tissue phosphoproteomes):* Peptides were loaded onto 50 cm fused silica columns packed in-house (ReproSil Pur C18-AQ, 1.9 µm particle size) and maintained at 60 °C using a column oven (Sonation, GmbH). Peptides were separated by reversed-phase chromatography using an Easy nLC 1000 coupled to a Q Exactive HF mass spectrometer (Thermo Fisher Scientific). Peptides were separated using a binary buffer system comprising 0.1% formic acid (buffer A) and 80% ACN plus 0.1% formic (buffer B), at a flow rate of 350 nl/min, with a gradient of 3–19% buffer B over 60 min followed by 19–41% buffer B over 30 min. Peptides were electrosprayed directly into the mass spectrometer by the application of 2.3 kV with a liquid junction union. The mass spectrometer was operated in data-dependent mode, performing survey scans of $3e^6$ ions at a resolution of 60,000 from 300-1,600 m/z, and the 5 most abundant precursors from the survey scan with charge state >1 and <5 were selected for fragmentation. Precursors were isolated with a window of 1.6 m/z and fragmented in the HCD cell with NCE of 25. Maximum ion fill times for the MS/MS scans were 120 ms, with a target of $4e^4$ ions (intensity threshold $3.3e^5$ ions). Fragment ions were analyzed with high resolution (15,000) in the Orbitrap mass analyzer, and dynamic exclusion was enabled with duration 45s.

*DDA-MS (GSK3i phosphoproteomes):* Peptides were loaded onto 50 cm fused silica columns packed in-house (ReproSil Pur C18-AQ, 1.9 µm particle size) and maintained at 60 °C using a column oven (Sonation, GmbH). Peptides were separated by reversed-phase chromatography using a Dionex U3000 HPLC coupled to a Q Exactive HF-X mass spectrometer (Thermo Fisher Scientific). Peptides were separated using a binary buffer system comprising 0.1% formic acid (buffer A) and 80% ACN plus 0.1% formic (buffer B), at a flow rate of 350 nl/min, with a gradient of 3–19% buffer B over 80 min followed by 19–41% buffer B over 40 min. Peptides were electrosprayed directly into the mass spectrometer by the application of 2.4 kV with a liquid junction union. The mass spectrometer was operated in data-dependent mode, performing survey scans of $3e^6$ ions at a resolution of 60,000 from 350-1,400 m/z, and the 10 most abundant precursors from the survey scan with charge state >1 and <5 were selected for fragmentation. Precursors were isolated with a window of 1.6 m/z and fragmented in the HCD cell with NCE of 27. Maximum ion fill times for the MS/MS scans were 50 ms, with a target

of $2e^4$ ions (intensity threshold $4e^5$ ions). Fragment ions were analyzed with high resolution (15,000) in the Orbitrap mass analyzer, and dynamic exclusion was enabled with duration 30s.

***MS RAW data processing***

*DDA:* RAW data was analyzed using MaxQuant [74] (v1.6.0.9, v1.6.1.0 and v1.6.17.0 for the adipose tissue phosphoproteomes, 3T3-L1 proteomes and GSK3i phosphoproteomes, respectively), searching against the *mus musculus* UniProt database (July 2017 and December 2019 releases for the tissue phosphoproteome and 3T3-L1 proteome, or GSK3i phosphoproteome). Default settings were used, with the addition of "Phospho(STY)" as a variable modification, and "match between runs" was turned on for all samples analyzed in the same runs.

*DIA:* RAW data was analyzed using Spectronaut (v14.11.210528.47784). Data were searched using directDIA against the Human UniProt Reference Proteome database (January 2021 release), with default settings (precursor and protein Qvalue cutoffs 0.01, Qvalue filtering, MS2 quantification), with "PTM localization" turned on. The PTM "Probability cutoff" was set to 0 and localization filtering was performed during downstream analysis. Spectronaut output tables were processed using the Peptide collapse (v1.4.2) plugin for Perseus [21,75].

***2-Deoxyglucose uptake assays in cultured cells***

Following 1.5 h serum-starvation in DMEM/0.2% BSA/1% GlutaMAX, cells were washed and incubated in pre-warmed Krebs–Ringer phosphate buffer containing 0.2% bovine serum albumin (BSA, Bovostar, Bovogen) (KRP buffer; 0.6 mM $Na_2HPO_4$, 0.4 mM $NaH_2PO_4$, 120 mM NaCl, 6 mM KCl, 1 mM $CaCl_2$, 1.2 mM $MgSO_4$ and 12.5 mM Hepes (pH 7.4)). Cells were stimulated with the indicated dose of insulin (typically 100 nM insulin) for 20 min or as indicated. To determine non-specific glucose uptake, 25 µM cytochalasin B (ethanol, Sigma Aldrich) was added to the wells before addition of 2-[3H]deoxyglucose (2DG) (PerkinElmer). During the final 5 min 2DG (0.25 µCi, 50 µM) was added to cells to measure steady-state rates of 2DG uptake. Following three washes with ice-cold PBS, cells were solubilised in PBS containing 1% (v/v) Triton X-100. Tracer uptake was quantified by liquid scintillation counting and data normalized for protein content.

***Assessment of plasma membrane GLUT4***

Plasma membrane GLUT4 was determined in 3T3-L1 adipocytes expressing the GLUT4 reporters HA-GLUT4 [71] (Fig. S4C) or HA-GLUT4-mRuby (Fig. 5A-B), or in wildtype 3T3-L1 (Fig. 5C-D). Cells were serum-starved for 2 h in DMEM/0.2% BSA/GlutaMAX in a CO2 incubator. Cells were stimulated with 0.5 or 100 nM insulin (as indicated) for indicated times. Cells were fixed in 4% PFA but not permeabilized. Residual PFA was quenched with 50 mM Glycine in PBS, followed by blocking in 5% Normal Swine Serum (NSS; Jackson ImmunoResearch) for 30 minutes at room temperature. The amount of HA-GLUT4 or HA-GLUT4-mRuby3 present at the plasma membrane was determined by the accessibility of the HA epitope to anti-HA antibody (Covance, clone 16B12). For wild type cells, GLUT4 present at the plasma membrane was labeled with human anti-GLUT4 antibody (LM048; [57]) (kindly provided by Joseph Rucker, Integral Molecular, PA, USA) that recognises an exofacial epitope in GLUT4. Cells were incubated with 20 µg/mL Alexa-488-conjugated anti-mouse IgG antibody (for anti-HA staining) or Alexa-488-conjugated anti-humanIgG antibody (for anti-

GLUT4 staining), followed by Alexa-488-conjugated secondary antibody (Thermo Fisher Scientific). Antibody incubations were performed in 2% NSS in PBS for 1 hour at room temperature.

*HA-GLUT4 cells:* Determination of total HA-GLUT4 was performed in a separate set of cells that underwent the same labeling procedure except that anti-HA staining was performed after permeabilization of the cells with 0.1% (w/v) saponin. Total HA-GLUT4 was measured separately for each experimental treatment group. Cells were stored in PBS containing 2.5% DABCO, 10% glycerol, pH 8.5. Fluorescence (excitation 485 nm/emission 520 nm) was measured using a fluorescent microtiter plate reader (FLUOstar Galaxy, BMG LABTECH). Surface HA-GLUT4 was expressed as a percentage of total HA-GLUT4.

*HA-GLUT4-mRuby3 and wild type cells:* Secondary antibody incubations also included Hoechst 33342 (Life Technologies) to label nuclei. Cells were stored in PBS containing 2.5% DABCO, 10% glycerol, pH 8.5 and imaged using the Opera Phenix High Content Screening System (Perkin Elmer). Confocal images (basal section for wild type cells, mid-section for HA-GLUT4-mRuby cells) were obtained using a 20x water objective (N.A 1.0), with 2-pixel binning, 9 images per well. Excitation wavelengths and emission filters used were as follows: endogenous surface GLUT4 and HA-tagged surface GLUT4: 488 nm, 500-550 nm; mRuby: 561 nm, 570-630 nm; Hoechst: 405 nm, 435-480 nm. Images were analyzed using Harmony phenoLOGIC Software (v4.9; Perkin Elmer) to quantify cell-associated anti-HA (Alexa-488), mRuby3 (as a measure of total cellular GLUT4) or anti-GLUT4 (Alexa-488) fluorescent signals. Surface HA-GLUT4-mRuby3 was expressed relative to total mRuby3 signal. Surface endogenous GLUT4 was expressed as raw Alexa-488 fluorescence.

***Phosphatase inhibitor treatment of 3T3-L1 adipocytes***

3T3-L1 adipocytes were serum-starved for 1.5 h and treated with or without calyculin A (50 nM, DMSO) (Cell Signaling Technologies) or okadaic acid (1 µM, $H_2O$) (Merck, Sigma) for 10 or 20 min in the absence of presence of insulin as indicated. In all cases the inhibitor was added at the same time and for the same duration as insulin. Vehicle controls were used as appropriate for each inhibitor.

***In vitro serine/threonine protein phosphatase activity assay***

Control 3T3-L1 adipocytes or adipocytes treated with insulin (CI), dexamethasone (Dex) or TNFα (TNF) to induce insulin resistance were serum started for 1.5 h and left unstimulated, or treated with 100 nM insulin for 10 min. Cells were then washed thrice with cold PBS and scraped in cold lysis buffer (20 mM Tris-HCl (pH 7.5), 1 mM Na-EGTA, 1% NP40 containing EDTA-free protease inhibitors (Roche)). Lysates were needle-homogenized and the fat cake removed by centrifugation. To assess global serine/threonine protein phosphatase activity, lysates were diluted up to 50 µL in lysis buffer before the addition of 50 µL of phosphatase assay buffer (20 mM Tris-HCl, pH 7.5, 5 mM NiCl (required for protein phosphatase 2B activity), 10 mM $MgCl_2$, 2 mM $MnCl_2$ (required for protein phosphatase 1 activity), 10 mM $CaCl_2$ (required for protein phosphatase 2B activity) and 10 mM pNPP). Reactions were incubated for 30 min at 37 ºC before being neutralized by the addition of 50 µL of 2 M NaOH and absorption at 405 nm immediately measured (Tecan Infinite M1000). A405 were blanked to reactions containing naïve lysis buffer. Phosphatase activity was calculated by determining

the amount of pNPP converted to NPP, using the molar extinction coefficient for pNPP (18000 $M^{-1}$ $cm^{-1}$), and normalizing to the amount of protein and reaction time. Different amounts of control lysate were included in each run to confirm linearity and control lysate was incubated with a phosphatase inhibitor cocktail (final concentrations: 2 mM sodium orthovanadate, 1 mM sodium pyrophosphate, 10 mM sodium fluoride) as a control for assay specificity.

***Animal details***

Eight-week-old male C57BL/6J mice were purchased from Australian BioResources (Moss Vale, Australia). The animals were kept in a temperature-controlled environment (22 ± 1°C) on a 12 h light/dark cycle with free access to food and water. Mice were split into three groups: 1) mice fed with standard lab diet (CHOW) (13% calories from fat, 22% calories from protein, and 65% calories from carbohydrate, 3.1 kcal/g; Gordon's Specialty Stock Feeds, Yanderra, Australia)for 14 d; 2) mice fed a high fat high sucrose diet (HFD; 47% of calories from fat (40% calories from lard), 21% calories from protein, and 32% calories from carbohydrates (16% calories from starch), 4.7 kcal/g) for 14 d; and 3) mice fed a HFD diet for 14 d, before returning to CHOW for 5 d. All experiments were carried out with the approval of the University of Sydney Animal Ethics Committee (2014/694), following guidelines issued by the National Health and Medical Research Council of Australia. All studies used at least twenty four mice [KT17] [DF18] per treatment group (n=12 saline treated, n=12 insulin-stimulated), and studies were performed over 4 separate days spanning two weeks. Due to low adipose tissue weight in chow-fed mice, lysates from adipose tissue from two mice were combined in order to obtain enough starting material for phosphoproteomics.

***Assessment of body composition***

Body composition of individual mice was assessed using the Echo-MRI 900 to determine lean mass, 24 h prior to euthanasia. Analysis was performed as per the manufacturer's specifications.

***In vivo insulin stimulation***

Mice were fasted from 1200 and experiments were carried out between 1800 and 2100 so that mice received insulin in line with their circadian rhythm [76,77]. Administration of saline/insulin and 2DG tracer via the hepatic portal vein was performed as previously described [78] with the following minor modifications. Mice were injected with 80 mg/kg lean mass (determined by Echo-MRI) pentobarbitone intraperitoneally. Following induction of anesthesia (approximately 15-20 min after injection), mice were placed on a heat pad (~30 °C), and the hepatic portal vein accessed via an incision to access the abdominal cavity. A bolus of saline or insulin (1 U/kg lean body mass) containing 5-10 μCi [3H]2DG tracer was administered via the hepatic portal vein. Blood samples were taken via the tail vein throughout the procedure to assess blood glucose concentrations and 2DG tracer. After 10 min, epididymal adipose tissue was excised, rinsed in ice-cold PBS and snap frozen in liquid nitrogen.

***2DG uptake assays in adipose tissue explants***

Assessment of insulin-stimulated 2DG uptake in adipose explants was performed as previously described [79] with minor modifications. Epididymal fat depots were excised from mice, transferred immediately to warm basal medium (DMEM/20 mM HEPES/2% bovine serum albumin (BSA, Bovostar, Bovogen), pH 7.4), and minced into fine pieces. Explants were

serum-starved for 2 h. The [$^3$H]2DG uptake assay was performed in Krebs–Ringer phosphate buffer containing 2% BSA (KRP buffer; 0.6 mM $Na_2HPO_4$, 0.4 mM $NaH_2PO_4$, 120 mM NaCl, 6 mM KCl, 1 mM $CaCl_2$, 1.2 mM $MgSO_4$ and 12.5 mM HEPES (pH 7.4)), whereby insulin and/or calyculin A (100 nM) was added for 20 min, and glucose transport was initiated by addition of [$^3$H]2DG (0.25 μCi, 50 μM) and [$^{14}$C]mannitol (Perkin Elmer, 0.036 μCi/sample) for the final 5 min of the assay to measure steady-state rates of 2DG uptake. The equivalent volume of vehicle (DMSO) was included for cells not treated with Calyculin A. Samples were assessed for radioactivity by scintillation counting and [$^{14}$C]mannitol was used to correct for extracellular [$^3$H]2DG. Fat explants were lysed in 100 nM NaOH for protein determination and assay normalization to total protein.

***2DG uptake assay in adipose tissue explants following GSK3 inhibition***

Fifteen 18-week old male C57Bl/6J were fed with standard lab diet (CHOW; 13% calories from fat, 22% calories from protein, and 65% calories from carbohydrate, 3.1 kcal/g; Gordon's Specialty Stock Feeds, Yanderra, Australia; 10 mice) or a high fat high sucrose diet (HFD; 45.5% of calories from fat (40% calories from lard), 20.5% calories from protein, and 34% calories from carbohydrate (14% calories from starch), 4.95 kcal/g; 5 mice) for 14d. In order to obtain enough starting material, epididymal fat depots from CHOW mice were combined, resulting in 5 pooled mice. Fat depots were then minced and divided into two explants per pooled mouse. After washing and 2 h incubation in DMEM/2% BSA/20 mM HEPES, pH 7.4, each pair of explants was exposed to 0.005 % (v/v) DMSO with or without 500 nM LY2090314 for 1 h. The 2DG uptake assay was then carried out as described above, allowing the assessment of the effects of both insulin and LY2090314 within each mouse by two-way repeated-measures ANOVA and Šídák's post-hoc tests using GraphPad Prism 9.3.1.

***Adipose tissue lysis***

Snap-frozen epididymal adipose tissue was heated for 5 min at 95 °C with shaking in SDC lysis buffer (4% Sodium Deoxycholate, 100 mM Tris pH 8.5). Lysates were sonicated (75% output power, 1x 15 s) and heated for an additional 5 min at 95 °C with shaking. Lysate was centrifuged for 20 min at 21,000xg at 0 °C to form a lipid layer. Clarified protein lysate was carefully collected without interfering with the upper lipid layer, and protein concentration was measured using BCA assay.

***Adipose tissue lysate processing to determine 2-[3H]deoxyglucose uptake***

Aliquots of lysed tissue in SDC buffer were treated with an equal volume of 1% trifluoroacetic acid to precipitate SDC and samples were centrifuged. Cleared lysates were transferred to a 96 well plate and dried using a vacuum centrifuge. Samples were resuspended in 10mM Tris-HCL pH8.5. Samples were transferred onto columns containing AG1-X8 resin to trap phosphorylated 2DG (2-[$^3$H] DG-6-P). Resin was washed three times with ddH2O, before 2-[$^3$H] DG-6-P was eluted with 2M NaCl, 1% trifluoroacetic acid. Eluants were assessed for radioactivity by liquid scintillation counting. Tracer in the blood was measured at 0, 1 and 10 min during the experiment and the average tracer count (DPM) between 1 and 10 min used to calculate the specific activity (DPM/mol glucose) and the glucose transport index [78]. Uptake data were normalized to tissue protein content.

***Phosphoproteome and proteome data processing and analysis***

**Filtering, imputation, and normalization**

The number of biological replicates per study are as follows. 3T3-L1 IR phosphoproteomics: CTRL unstimulated (BAS) = 6; CI, DEX, TNF, MPQ, and AA BAS = 4; CTRL insulin stimulated (INS) = 6; CI, DEX, TNF, MPQ, and AA INS = 4. 3T3-L1 IR proteomics: CTRL BAS = 5, CI BAS = 3, DEX BAS = 4, TNF BAS = 3, MPQ BAS = 4, AA BAS = 4, CTRL INS = 5, CI INS = 4, DEX INS = 4, TNF INS = 4, MPQ INS = 4, AA INS = 4. Mouse phosphoproteomics: CHOW BAS = 12, HFD BAS = 12, REV BAS = 12, CHOW INS = 12, HFD INS = 12, REV INS = 12. GSK3i phosphoproteomics: Basal = 4, GSK3i = 4.

Phosphopeptides/proteins that were quantified in fewer than eight replicates in the 3T3-L1 IR proteomics and mouse phosphoproteomics studies were removed. Additionally, proteins that were not quantified in any CTRL replicates were removed from the 3T3-L1 IR proteomics study. Following filtering, LFQ intensities were log2-transformed and median normalized. In the 3T3-L1 and mouse IR phosphoproteomics studies, imputation was first performed within each model/diet including CTRL and CHOW. Briefly, if phosphopeptide X was poorly quantified in BAS and well quantified in INS for model Y, or vice versa, all missing values in BAS were imputed by sampling from a downshifted normal distribution: $N(val_{min} - 1, sigma^2_{wellquant})$, where $val_{min}$ is the minimum intensity for phosphopeptide X across all conditions, and $sigma_{wellquant}$ is the standard deviation for phosphopeptide X within INS replicates for model Y. The same technique was applied to the GSK3i phosphoproteome study, using Basal and GSK3i-treated instead of BAS and INS. The criteria for "poorly quantified" and "well quantified" were respectively as follows. 3T3-L1 phosphoproteomics: 0 quantifications, >= 5/6 quantifications (CTRL) or 4/4 quantifications (CI, DEX, TNF, MPQ, AA). Mouse phosphoproteomics: 0/12 quantifications, >= 7/12 quantifications. GSK3i phosphoproteomics: <= 1/4 quantification, >= 3/4 quantifications. For GSK3i phosphoproteomics, in the case that only 1 value was quantified in Basal but was higher than the mean of GSK3i values (or vice versa) imputation was not performed. A second step of imputation was performed on the mouse and GSK3i phosphoproteomics studies, where if a phosphopeptide was quantified at least five (mouse) or three (GSK3i) times in a given diet and treatment, the remaining missing values were imputed by sampling from a normal distribution: $N(mu_{self}, sigma^2_{self})$, where $mu_{self}$ and $sigma_{self}$ are the mean and standard deviation within that diet and treatment.

**Statistical analysis**

*3T3-L1 IR phosphoproteomics:* First, to characterize the response to insulin in insulin sensitive cells, t-tests were performed (base R function "t.test") comparing CTRL BAS to CTRL INS for all phosphopeptides that were quantified at least twice in both conditions. p-values were adjusted by the Benjamini-Hochberg procedure. Next, CTRL INS values were normalized to CTRL BAS by subtracting the CTRL BAS median. This was repeated in each insulin resistance model, and the resulting insulin responses were compared by ANOVA (base R function "aov") for all phosphopeptides quantified at least twice in BAS and INS for both CTRL and one or more models. For phosphopeptides that were significant in the ANOVA after p-value adjustment, Dunnett's post-hoc tests ("glht" function from "multcomp") were performed to compare the insulin response in each model to that of CTRL cells, and the resulting p-values were adjusted within each model.

*3T3-L1 IR proteomics:* First, BAS and INS values were compared within each group by t-tests, followed by Benjamini-Hochberg adjustment. BAS and INS values were then pooled within each group, and groups were compared by ANOVA. For proteins that were significant in the ANOVA after Benjamini-Hochberg p-value adjustment, Dunnett's post-hoc tests were performed to compare each insulin resistance model to CTRL cells, and the resulting p-values were adjusted within each model.

*Mouse adipose tissue phosphoproteomics:* To characterize the response to insulin within each diet, BAS and INS values were compared using empirical Bayes moderated t-tests implemented in the R package "Limma" [80,81]. p-values were adjusted within each diet by the Benjamini-Hochberg procedure.

*GSK3i phosphoproteomics:* To assess the effect of GSK3 inhibition, Basal and GSK3i values were compared by standard t-tests for all phosphopeptides quantified at least twice in each condition, followed by Benjamini-Hochberg p-value adjustment.

**Insulin-regulated, defective, and emergent phosphopeptides**

In the 3T3-L1 IR and mouse phosphoproteomics studies, insulin-regulated phosphopeptides were defined as those where the difference between BAS and INS in CTRL or CHOW was significant (adj. $p < 0.05$) and of sufficient magnitude (log2 INS/BAS > 0.58 corresponding to INS/BAS > 1.5, or log2 INS/BAS < -0.58 corresponding to INS/BAS < 0.5).

Defective phosphopeptides were defined as those that responded to insulin under insulin sensitive conditions but failed to respond to insulin in insulin resistance. In the 3T3-L1 IR phosphoproteomics study, an insulin-regulated phosphopeptide was considered defective in a given model if its insulin response in that model was significantly different to CTRL (adj. $p < 0.05$) and sufficiently small (log2 INS/BAS < 0.58 for CTRL up-regulated phosphopeptides, log2 INS/BAS > -0.58 for CTRL down-regulated phosphopeptides). In the mouse phosphoproteomics study, a phosphopeptide was considered defective in HFD if it was insulin-regulated in CHOW but not HFD (HFD log2 INS/BAS < 0.58 for CHOW up-regulated phosphopeptides, log2 INS/BAS > -0.58 for CHOW down-regulated phosphopeptides).

Emergent phosphopeptides were defined as those that did not respond to insulin under insulin sensitive conditions but did respond in insulin resistance. In the 3T3-L1 IR phosphoproteomics study, a phosphopeptide was considered emergent in a given model if the insulin response in that model was of sufficient magnitude (log2 INS/BAS > 0.58 or < -0.58) and significantly different to CTRL (adj. $p < 0.05$), and if the phosphopeptide did not respond to insulin in CTRL (adj. $p >= 0.05$, -0.58 <= log2 INS/BAS <= 0.58). In the mouse phosphoproteomics study, a phosphopeptide was considered emergent if it was regulated by insulin in HFD (adj. $p < 0.05$, log2 INS/BAS > 0.58 or < -0.58) but not in CHOW (adj. $p >= 0.05$, -0.58 <= log2 INS/BAS <= 0.58).

In the 3T3-L1 IR phosphoproteomics study, defective phosphopeptides were further analyzed to attribute defects to changes in the basal or insulin-stimulated states. First, two ANOVAs were performed for each defective phosphopeptide using either BAS or INS values, comparing only CTRL and the specific models that were defective. Dunnett's post-hoc tests were

performed on phosphopeptides that were significant in the ANOVA after Benjamini-Hochberg p-value adjustment, and the resulting Dunnett's p-values were adjusted within each model. For a given phosphopeptide X that was up-regulated by insulin in CTRL and defective in model Y, an insulin defect was declared if the difference in INS values between model Y and CTRL was significant (adj. $p < 0.05$), of sufficient magnitude (FC > 1.5), and changed in the correct direction (model Y < CTRL). Similar filtering was performed for down-regulated phosphopeptides and for identifying basal defects.

**Kinase-based analysis**

Mouse kinase-substrate annotations were extracted from PhosphositePlus([28], version: Dec 2 2019) and mapped into the 3T3-L1 IR phosphoproteome by matching uniprots and phosphosite positions. Annotations for kinase isoforms were merged, for example Akt1, Akt2, and Akt3 were merged, and GSK3a and GSK3b were merged. Kinase substrate enrichment analysis (KSEA) was then performed with the "ksea_batchKinases" function from the R package "ksea" [27], using the log2 INS/BAS fold changes from each model. Kinases with fewer than 10 substrates quantified in each model were considered irrelevant and were excluded. 1000 permutations were performed to determine empirical p-values which were then adjusted within each model by the Benjamini-Hochberg procedure.

**Pathway enrichment**

Mouse Gene Ontology(GO) Biological Processes and Cellular Compartments were extracted using the R package "org.Mm.eg.db" ([83], version 3.12.0) and KEGG canonical pathways were downloaded from the MSigDB collections ([84,85], version 7.2). Pathway enrichment was performed by either one-sided Fisher's exact test or gene set test using the "geneSetTest" function from the R package "limma" [81]. In the case of gene set test, log2 Model/CTRL fold changes were provided as the enrichment statistic and 9999 random samples were used to determine empirical p-values. In order to separately identify up-regulated and down-regulated pathways separate tests were performed using "up" and "down" as the alternative hypothesis.

Functional protein-protein interaction networks were constructed and analyzed using the STRING web app (https://string-db.org/, version 11.0b). First, two networks were constructed using all proteins either up-regulated or down-regulated in two or more models compared to CTRL cells. Interaction scores were calculated using the Experimental, Database, and Coexpression evidence channels as these were considered the most relevant, and only high-confidence interactions were retained (score > 0.7). Markov clustering was then performed using the default inflation parameter value of 3, and clusters containing ten or more proteins were retained for further analysis. To functionally characterize these clusters pathway enrichment was performed in STRING using the KEGG and Reactome pathways.

**GSK3i substrate identification**

In the GSK3i phosphoproteomics study, GSK3 substrate phosphopeptides were defined as those that were decreased by GSK3 inhibition (adj. $p < 0.05$, log2 GSK3i/Basal < -0.58) and matched the GSK3 substrate motif. To phosphorylate a serine/threonine GSK3 ordinarily requires a priming phosphoserine/threonine four residues downstream, however some GSK3 substrates have a gap of three [86] or five residues [52], implying the general substrate motif pS/T X(2-4) *pS/T, where * indicates the priming phosphosite. Hence a given

phosphoserine/threonine matched the GSK3 motif if a priming phosphoserine/threonine was identified 3-5 residues downstream in our phosphoproteomics data or in the PhosphositePlus database ([28], version: Jan 27 2021).

**Canonical insulin signaling proteins**

Canonical insulin proteins were compiled as previously described [87] by compiling annotations from Gene Ontology (GO), Kyoto Encyclopedia of Genes and Genomes, Reactome, and our previous publication[18].

## References

1. James, D. E., Stöckli, J. & Birnbaum, M. J. The aetiology and molecular landscape of insulin resistance. *Nat. Rev. Mol. Cell Biol.* (2021) doi:10.1038/s41580-021-00390-6.
2. Turner, N. *et al.* Distinct patterns of tissue-specific lipid accumulation during the induction of insulin resistance in mice by high-fat feeding. *Diabetologia* **56**, 1638–1648 (2013).
3. Fazakerley, D. J. *et al.* Mitochondrial CoQ deficiency is a common driver of mitochondrial oxidants and insulin resistance. *Elife* **7**, (2018).
4. Abel, E. D. *et al.* Adipose-selective targeting of the GLUT4 gene impairs insulin action in muscle and liver. *Nature* **409**, 729–733 (2001).
5. Czech, M. P. Mechanisms of insulin resistance related to white, beige, and brown adipocytes. *Mol Metab* **34**, 27–42 (2020).
6. Humphrey, S. J., James, D. E. & Mann, M. Protein Phosphorylation: A Major Switch Mechanism for Metabolic Regulation. *Trends Endocrinol. Metab.* **26**, 676–687 (2015).
7. Hotamisligil, G. S., Shargill, N. S. & Spiegelman, B. M. Adipose expression of tumor necrosis factor-alpha: direct role in obesity-linked insulin resistance. *Science* **259**, 87–91 (1993).
8. Rizza, R. A., Mandarino, L. J., Genest, J., Baker, B. A. & Gerich, J. E. Production of insulin resistance by hyperinsulinaemia in man. *Diabetologia* **28**, 70–75 (1985).
9. Kusunoki, M., Cooney, G. J., Hara, T. & Storlien, L. H. Amelioration of high-fat feeding-induced insulin resistance in skeletal muscle with the antiglucocorticoid RU486. *Diabetes* **44**, 718–720 (1995).
10. Chavez, J. A. *et al.* A role for ceramide, but not diacylglycerol, in the antagonism of insulin signal transduction by saturated fatty acids. *J. Biol. Chem.* **278**, 10297–10303 (2003).

11. Yu, C. *et al.* Mechanism by which fatty acids inhibit insulin activation of insulin receptor substrate-1 (IRS-1)-associated phosphatidylinositol 3-kinase activity in muscle. *J. Biol. Chem.* **277**, 50230–50236 (2002).

12. Kelley, D. E., He, J., Menshikova, E. V. & Ritov, V. B. Dysfunction of mitochondria in human skeletal muscle in type 2 diabetes. *Diabetes* **51**, 2944–2950 (2002).

13. Houstis, N., Rosen, E. D. & Lander, E. S. Reactive oxygen species have a causal role in multiple forms of insulin resistance. *Nature* **440**, 944–948 (2006).

14. Ozcan, U. *et al.* Endoplasmic reticulum stress links obesity, insulin action, and type 2 diabetes. *Science* **306**, 457–461 (2004).

15. Copps, K. D. & White, M. F. Regulation of insulin sensitivity by serine/threonine phosphorylation of insulin receptor substrate proteins IRS1 and IRS2. *Diabetologia* **55**, 2565–2582 (2012).

16. Fazakerley, D. J., Krycer, J. R., Kearney, A. L., Hocking, S. L. & James, D. E. Muscle and adipose tissue insulin resistance: malady without mechanism? *J. Lipid Res.* **60**, 1720–1732 (2019).

17. Krüger, M. *et al.* Dissection of the insulin signaling pathway via quantitative phosphoproteomics. *Proc. Natl. Acad. Sci. U. S. A.* **105**, 2451–2456 (2008).

18. Humphrey, S. J. *et al.* Dynamic adipocyte phosphoproteome reveals that Akt directly regulates mTORC2. *Cell Metab.* **17**, 1009–1020 (2013).

19. Batista, T. M. *et al.* A Cell-Autonomous Signature of Dysregulated Protein Phosphorylation Underlies Muscle Insulin Resistance in Type 2 Diabetes. *Cell Metab.* **32**, 844–859.e5 (2020).

20. Humphrey, S. J., Karayel, O., James, D. E. & Mann, M. High-throughput and high-sensitivity phosphoproteomics with the EasyPhos platform. *Nat. Protoc.* **13**, 1897–1916 (2018).

21. Bekker-Jensen, D. B. *et al.* Rapid and site-specific deep phosphoproteome profiling by data-independent acquisition without the need for spectral libraries. *Nat. Commun.* **11**, 787 (2020).

22. Hoehn, K. L. *et al.* Insulin resistance is a cellular antioxidant defense mechanism. *Proc. Natl. Acad. Sci. U. S. A.* **106**, 17787–17792 (2009).

23. Fazakerley, D. J. *et al.* Mitochondrial oxidative stress causes insulin resistance without disrupting oxidative phosphorylation. *J. Biol. Chem.* **293**, 7315–7328 (2018).

24. Lo, K. A. *et al.* Analysis of in vitro insulin-resistance models and their physiological relevance to in vivo diet-induced adipose insulin resistance. *Cell Rep.* **5**, 259–270 (2013).

25. Szklarczyk, D., Gable, A. L., Nastou, K. C. & Lyon, D. The STRING database in 2021: customizable protein–protein networks, and functional characterization of user-uploaded gene/measurement sets. *Nucleic acids* (2021).

26. Yang, P. *et al.* Multi-omic Profiling Reveals Dynamics of the Phased Progression of Pluripotency. *Cell Syst* **8**, 427–445.e10 (2019).

27. Hernandez-Armenta, C., Ochoa, D., Gonçalves, E., Saez-Rodriguez, J. & Beltrao, P. Benchmarking substrate-based kinase activity inference using phosphoproteomic data. *Bioinformatics* **33**, 1845–1851 (2017).

28. Hornbeck, P. V. *et al.* PhosphoSitePlus, 2014: mutations, PTMs and recalibrations. *Nucleic Acids Res.* **43**, D512–20 (2015).

29. Haeusler, R. A., McGraw, T. E. & Accili, D. Biochemical and cellular properties of insulin receptor signalling. *Nat. Rev. Mol. Cell Biol.* **19**, 31–44 (2018).

30. Gehart, H., Kumpf, S., Ittner, A. & Ricci, R. MAPK signalling in cellular metabolism: stress or wellness? *EMBO Rep.* **11**, 834–840 (2010).

31. Jope, R. S. & Johnson, G. V. W. The glamour and gloom of glycogen synthase kinase-3. *Trends Biochem. Sci.* **29**, 95–102 (2004).

32. Ruiz-Alcaraz, A. J. *et al.* Obesity-induced insulin resistance in human skeletal muscle is characterised by defective activation of p42/p44 MAP kinase. *PLoS One* **8**, e56928 (2013).

33. Cusi, K. *et al.* Insulin resistance differentially affects the PI 3-kinase– and MAP kinase–mediated signaling in human muscle. *Journal of Clinical Investigation* vol. 105 311–320 (2000).

34. Ozaki, K.-I. *et al.* Targeting the ERK signaling pathway as a potential treatment for insulin resistance and type 2 diabetes. *Am. J. Physiol. Endocrinol. Metab.* **310**, E643–E651 (2016).

35. Bashan, N. *et al.* Mitogen-activated protein kinases, inhibitory-kappaB kinase, and insulin signaling in human omental versus subcutaneous adipose tissue in obesity. *Endocrinology* **148**, 2955–2962 (2007).

36. Bouzakri, K. *et al.* Reduced activation of phosphatidylinositol-3 kinase and increased serine 636 phosphorylation of insulin receptor substrate-1 in primary culture of skeletal muscle cells from

patients with type 2 diabetes. *Diabetes* **52**, 1319–1325 (2003).

37. Carlson, C. J., Koterski, S., Sciotti, R. J., Poccard, G. B. & Rondinone, C. M. Enhanced basal activation of mitogen-activated protein kinases in adipocytes from type 2 diabetes: potential role of p38 in the downregulation of GLUT4 expression. *Diabetes* **52**, 634–641 (2003).
38. Lalioti, V. *et al.* The atypical kinase Cdk5 is activated by insulin, regulates the association between GLUT4 and E-Syt1, and modulates glucose transport in 3T3-L1 adipocytes. *Proc. Natl. Acad. Sci. U. S. A.* **106**, 4249–4253 (2009).
39. Cheng, X. *et al.* Pacer Is a Mediator of mTORC1 and GSK3-TIP60 Signaling in Regulation of Autophagosome Maturation and Lipid Metabolism. *Mol. Cell* **73**, 788–802.e7 (2019).
40. Charvet, C. *et al.* Phosphorylation of Tip60 by GSK-3 determines the induction of PUMA and apoptosis by p53. *Mol. Cell* **42**, 584–596 (2011).
41. Fujii, K. *et al.* Negative control of apoptosis signal-regulating kinase 1 through phosphorylation of Ser-1034. *Oncogene* **23**, 5099–5104 (2004).
42. Bian, L. *et al.* Variants in ASK1 are associated with skeletal muscle ASK1 expression, in vivo insulin resistance, and type 2 diabetes in Pima Indians. *Diabetes* **59**, 1276–1282 (2010).
43. Baumann, C. A. *et al.* CAP defines a second signalling pathway required for insulin-stimulated glucose transport. *Nature* **407**, 202–207 (2000).
44. Meima, M. E., Webb, B. A., Witkowska, H. E. & Barber, D. L. The sodium-hydrogen exchanger NHE1 is an Akt substrate necessary for actin filament reorganization by growth factors. *J. Biol. Chem.* **284**, 26666–26675 (2009).
45. Su, Z., Deshpande, V., James, D. E. & Stöckli, J. Tankyrase modulates insulin sensitivity in skeletal muscle cells by regulating the stability of GLUT4 vesicle proteins. *J. Biol. Chem.* **293**, 8578–8587 (2018).
46. Yeh, T.-Y. J., Sbodio, J. I., Tsun, Z.-Y., Luo, B. & Chi, N.-W. Insulin-stimulated exocytosis of GLUT4 is enhanced by IRAP and its partner tankyrase. *Biochem. J* **402**, 279–290 (2007).
47. Kim, J. J., Lipatova, Z. & Segev, N. TRAPP Complexes in Secretion and Autophagy. *Front Cell Dev Biol* **4**, 20 (2016).
48. Zhou, Q. L. *et al.* A novel pleckstrin homology domain-containing protein enhances insulin-stimulated Akt phosphorylation and GLUT4 translocation in adipocytes. *J. Biol. Chem.* **285**,

27581–27589 (2010).

49. Lawrence, J. C., Jr, Hiken, J. F. & James, D. E. Stimulation of glucose transport and glucose transporter phosphorylation by okadaic acid in rat adipocytes. *J. Biol. Chem.* **265**, 19768–19776 (1990).
50. Engler, T. A. *et al.* Substituted 3-Imidazo[1,2-a]pyridin-3-yl- 4-(1,2,3,4-tetrahydro-[1,4]diazepino- [6,7,1-hi]indol-7-yl)pyrrole-2,5-diones as Highly Selective and Potent Inhibitors of Glycogen Synthase Kinase-3. *Journal of Medicinal Chemistry* vol. 47 3934–3937 (2004).
51. MacAulay, K. & Woodgett, J. R. Targeting glycogen synthase kinase-3 (GSK-3) in the treatment of Type 2 diabetes. *Expert Opin. Ther. Targets* **12**, 1265–1274 (2008).
52. Cole, A. R. *et al.* GSK-3 phosphorylation of the Alzheimer epitope within collapsin response mediator proteins regulates axon elongation in primary neurons. *J. Biol. Chem.* **279**, 50176–50180 (2004).
53. Yoshimura, T. *et al.* GSK-3beta regulates phosphorylation of CRMP-2 and neuronal polarity. *Cell* **120**, 137–149 (2005).
54. Fazakerley, D. J. *et al.* Proteomic Analysis of GLUT4 Storage Vesicles Reveals Tumor Suppressor Candidate 5 (TUSC5) as a Novel Regulator of Insulin Action in Adipocytes. *J. Biol. Chem.* **290**, 23528–23542 (2015).
55. Beaton, N. *et al.* TUSC5 regulates insulin-mediated adipose tissue glucose uptake by modulation of GLUT4 recycling. *Mol Metab* **4**, 795–810 (2015).
56. Duan, X. *et al.* Trafficking regulator of GLUT4-1 (TRARG1) is a GSK3 substrate. *bioRxiv* 2020.12.07.415257 (2022).
57. Tucker, D. F. *et al.* Isolation of state-dependent monoclonal antibodies against the 12-transmembrane domain glucose transporter 4 using virus-like particles. *Proc. Natl. Acad. Sci. U. S. A.* **115**, E4990–E4999 (2018).
58. Ring, D. B. *et al.* Selective glycogen synthase kinase 3 inhibitors potentiate insulin activation of glucose transport and utilization in vitro and in vivo. *Diabetes* **52**, 588–595 (2003).
59. Dokken, B. B., Sloniger, J. A. & Henriksen, E. J. Acute selective glycogen synthase kinase-3 inhibition enhances insulin signaling in prediabetic insulin-resistant rat skeletal muscle. *Am. J. Physiol. Endocrinol. Metab.* **288**, E1188–94 (2005).

60. Henriksen, E. J. & Teachey, M. K. Short-term in vitro inhibition of glycogen synthase kinase 3 potentiates insulin signaling in type I skeletal muscle of Zucker Diabetic Fatty rats. *Metabolism* **56**, 931–938 (2007).

61. Rao, R. *et al.* Glycogen synthase kinase 3 inhibition improves insulin-stimulated glucose metabolism but not hypertension in high-fat-fed C57BL/6J mice. *Diabetologia* **50**, 452–460 (2007).

62. Needham, E. J., Parker, B. L., Burykin, T., James, D. E. & Humphrey, S. J. Illuminating the dark phosphoproteome. *Sci. Signal.* **12**, (2019).

63. Sugiyama, N., Imamura, H. & Ishihama, Y. Large-scale Discovery of Substrates of the Human Kinome. *Sci. Rep.* **9**, 10503 (2019).

64. Ochoa, D. *et al.* The functional landscape of the human phosphoproteome. *Nat. Biotechnol.* **38**, 365–373 (2020).

65. Viéitez, C. *et al.* High-throughput functional characterization of protein phosphorylation sites in yeast. *Nat. Biotechnol.* **40**, 382–390 (2022).

66. Attwood, M. M., Fabbro, D., Sokolov, A. V., Knapp, S. & Schiöth, H. B. Trends in kinase drug discovery: targets, indications and inhibitor design. *Nat. Rev. Drug Discov.* **20**, 839–861 (2021).

67. Sacco, F. *et al.* Phosphoproteomics Reveals the GSK3-PDX1 Axis as a Key Pathogenic Signaling Node in Diabetic Islets. *Cell Metab.* **29**, 1422–1432.e3 (2019).

68. Benzler, J. *et al.* Hypothalamic glycogen synthase kinase 3β has a central role in the regulation of food intake and glucose metabolism. *Biochem. J* **447**, 175–184 (2012).

69. Su, Z. *et al.* Global redox proteome and phosphoproteome analysis reveals redox switch in Akt. *Nat. Commun.* **10**, 5486 (2019).

70. Santos, C. X. C. *et al.* Targeted redox inhibition of protein phosphatase 1 by Nox4 regulates eIF2α-mediated stress signaling. *EMBO J.* **35**, 319–334 (2016).

71. Govers, R., Coster, A. C. F. & James, D. E. Insulin increases cell surface GLUT4 levels by dose dependently discharging GLUT4 into a cell surface recycling pathway. *Mol. Cell. Biol.* **24**, 6456–6466 (2004).

72. Hoehn, K. L. *et al.* IRS1-independent defects define major nodes of insulin resistance. *Cell Metab.* **7**, 421–433 (2008).

73. Kulak, N. A., Pichler, G., Paron, I., Nagaraj, N. & Mann, M. Minimal, encapsulated proteomic-sample processing applied to copy-number estimation in eukaryotic cells. *Nat. Methods* **11**, 319–324 (2014).

74. Cox, J. & Mann, M. MaxQuant enables high peptide identification rates, individualized p.p.b.-range mass accuracies and proteome-wide protein quantification. *Nat. Biotechnol.* **26**, 1367–1372 (2008).

75. Tyanova, S. *et al.* The Perseus computational platform for comprehensive analysis of (prote)omics data. *Nat. Methods* **13**, 731–740 (2016).

76. Robles, M. S., Humphrey, S. J. & Mann, M. Phosphorylation Is a Central Mechanism for Circadian Control of Metabolism and Physiology. *Cell Metab.* **25**, 118–127 (2017).

77. Small, L. *et al.* Reduced insulin action in muscle of high fat diet rats over the diurnal cycle is not associated with defective insulin signaling. *Mol Metab* **25**, 107–118 (2019).

78. Fazakerley, D. J. *et al.* Insulin Tolerance Test under Anaesthesia to Measure Tissue-specific Insulin-stimulated Glucose Disposal. *Bio Protoc* **9**, e3146 (2019).

79. Tan, S.-X. *et al.* Selective insulin resistance in adipocytes. *J. Biol. Chem.* **290**, 11337–11348 (2015).

80. Smyth, G. K. Linear models and empirical bayes methods for assessing differential expression in microarray experiments. *Stat. Appl. Genet. Mol. Biol.* **3**, Article3 (2004).

81. Ritchie, M. E. *et al.* limma powers differential expression analyses for RNA-sequencing and microarray studies. *Nucleic Acids Res.* **43**, e47 (2015).

82. Amanchy, R. *et al.* A curated compendium of phosphorylation motifs. *Nat. Biotechnol.* **25**, 285–286 (2007).

83. Carlson, M. org. Mm. eg. db: Genome wide annotation for Mouse. R package version 3.2. 3. *Bioconductor. London, United Kingdom: Genome Biology (BMC)* (2019).

84. Subramanian, A. *et al.* Gene set enrichment analysis: a knowledge-based approach for interpreting genome-wide expression profiles. *Proc. Natl. Acad. Sci. U. S. A.* **102**, 15545–15550 (2005).

85. Liberzon, A. *et al.* Molecular signatures database (MSigDB) 3.0. *Bioinformatics* **27**, 1739–1740 (2011).

86. Singh, S. A. *et al.* FLEXIQinase, a mass spectrometry–based assay, to unveil multikinase mechanisms. *Nat. Methods* **9**, 504–508 (2012).

87. Needham, E. J. *et al.* Personalized phosphoproteomics identifies functional signaling. *Nat. Biotechnol.* (2021) doi:10.1038/s41587-021-01099-9.